Amplification and phase-synchronization of superconducting fluctuations in driven $YBa_2Cu_3O_{6+x}$

A. von Hoegen[1], M. Fechner[1], M. Först[1], N. Taherian[1], E. Rowe[1], A. Ribak[1], J. Porras[2], B. Keimer[2], M. Michael[3], E. Demler[3], A. Cavalleri[1,4]

[1] *Max Planck Institute for the Structure and Dynamics of Matter, Hamburg, Germany*

[2] *Max Planck Institute for Solid State Research, Stuttgart, Germany*

[3] *Department of Physics, Harvard University, USA*

[4] *Department of Physics, University of Oxford, UK*

Supplemental Material

S1. Nonlinear phonon-phonon coupling

The phonon spectrum of the centrosymmetric ortho-II structure of $YBa_2Cu_3O_{6.5}$ consists of 73 non-translational modes at the Brillouin zone center. The most relevant phonon modes for *c*-axis polarized THz and mid-infrared excitation are 13 infrared-active B_{1u} modes and 11 Raman-active A_g modes.

The full lattice potential V_{lattice} consists of three distinct contributions.[1,2]

1. The harmonic potential of each phonon mode

$$V_{\mathrm{harm}} = \sum \frac{\omega_{\mathrm{i}}^2}{2} Q_{\mathrm{i}}^2, \tag{1.1}$$

with ω_i and Q_i representing the eigenfrequency and coordinate of the i-th mode, respectively.

2. The anharmonic potential containing higher-order terms of the phonon coordinates and combinations of different phonon modes

$$V_{\mathrm{anharm}} = \sum g_{\mathrm{ijk}} Q_{\mathrm{i}} Q_{\mathrm{j}} Q_{\mathrm{k}} + \sum f_{\mathrm{iklm}} Q_{\mathrm{i}} Q_{\mathrm{k}} Q_{\mathrm{l}} Q_{\mathrm{m}}, \tag{1.2}$$

with g_{ijk} and f_{iklm} being the third-order and fourth-order anharmonic coefficients.

3. The coupling of the resonantly driven infrared-active B_{1u} phonon mode (with coordinate Q_{drive} and eigenfrequency ω_{drive}) to an external electric field E_{field}

$$V_{\mathrm{field}} = \sum Z^*_{\mathrm{drive}} Q_{\mathrm{drive}} E_{\mathrm{field}}\,, \tag{1.3}$$

with Z^*_{drive} representing the mode effective charge.

The crystal lattice dynamics are then determined by the equations of motion for each phonon mode, given by

$$\ddot{Q}_{\mathrm{i}} + 2\gamma_{\mathrm{i}} \dot{Q}_{\mathrm{i}} + \nabla_{Q_{\mathrm{i}}} (V_{\mathrm{harm}} + V_{\mathrm{anharm}} + V_{\mathrm{field}}) = 0. \tag{1.4}$$

Here γ_i is a phenomenological damping term, which accounts for contributions to the finite lifetime not already considered within the anharmonic potential. The equations are restricted to phonon modes at the Brillouin zone center, due to the negligible momentum of long-wavelength THz light.

First, we consider the resonant excitation of the infrared-active B_{1u} phonon Q_{drive} by the mid-IR pulses of electric field E_{field} oscillating at the frequency ω_{drive} of this mode. The equation of motion then reduces to

$$\ddot{Q}_{\mathrm{drive}} + \gamma \dot{Q}_{\mathrm{drive}} + \omega_{\mathrm{drive}}^2 Q_{\mathrm{drive}} = Z_{\mathrm{drive}}^* Q_{\mathrm{drive}} E_{\mathrm{field}}$$

and predicts a linear scaling of the mode with the electric field strength. Indeed, the measured amplitude of the optically driven phonons Q_{drive}, shown in Figure S1 (dashed line), follows this dependence for peak electric fields < 5MV/cm. However, saturation sets in at larger field strengths. This can be understood by considering anharmonicity of this mode described by a fourth-order term $f_4 Q_{drive}^4$ in the energy potential that renormalizes the frequency of the oscillator as $\omega^2(Q_{drive}) = \omega_{drive}^2 - f_4 Q_{drive}^2$ at large amplitudes and results in a less efficient drive by the pump electric field.

A minimal set of parameters used to calculate the oscillation amplitudes of the two driven apical oxygen phonon modes is listed in the following table.

$\omega_{\mathrm{drive}}/2\pi$ (THz)	γ (THz)	f_4 (meV/u^{2}Å^4)	Z_{drive}^* (e/u$^{0.5}$)
17.0	2.9	55	0.84
20.0	2.4	101	0.78

Next, we consider the impact of the third-order terms in V_{anharm}. Only the 11 A_g modes fulfill the symmetry requirements to exhibit third-order coupling to the driven B_{1u} mode [3]. To

simplify the discussion, we consider coupling between the driven mode and a single A_g mode. The equations of motions then reduce to

$$\ddot{Q}_{\mathrm{drive}} + \gamma \dot{Q}_{\mathrm{drive}} + \omega_{\mathrm{drive}}^2 Q_{\mathrm{drive}} + 2gQ_{\mathrm{drive}}Q_{\mathrm{Ag}} = Z_{\mathrm{drive}}^* Q_{\mathrm{drive}} E_{\mathrm{field}} \qquad (1.5)$$

$$\ddot{Q}_{\mathrm{Ag}} + \gamma_{\mathrm{Ag}} \dot{Q}_{\mathrm{Ag}} + \omega_{\mathrm{Ag}}^2 Q_{\mathrm{Ag}} + gQ_{\mathrm{drive}}^2 = 0. \qquad (1.6)$$

They describe a process known as ionic Raman scattering which entails a transient displacement and superimposed oscillations of the Q_{Ag} coordinate [3,4].

As detailed in the main text, coherent non-polar A_g-symmetry modes can be observed by Raman scattering of a femtosecond probe pulse in the time delay dependent reflectivity changes. The coherent component of the time-resolved reflectivity $\Delta R(t)$, shown in Figure 1b of the main text, is shown for $YBa_2Cu_3O_{6.48}$ and $YBa_2Cu_3O_{6.65}$ together with their Fourier transforms in Fig. S2a-d. The frequencies of the observed modes at 3.7, 4.2 and 4.5 THz agree with continuous-wave Raman scattering experiments and theoretical predictions of the same compound. The real space motions of these impulsively driven modes, which involve oscillation of the in-plane Cu atoms, are depicted in Fig. S2e. The measured amplitude of these Raman-active modes scales quadratically with the amplitude of the optically driven phonons Q_{drive}, as shown in Fig. S2f.

The results agree with the calculated response of the Raman-active modes, shown for $YBa_2Cu_3O_{6.5}$ in Fig. S3, which are driven by the third-order nonlinear coupling to the resonantly driven apical oxygen phonons $\sim Q_{\mathrm{drive}}^2 Q_{\mathrm{Ag}}$.

Next, we consider the lattice dynamics induced by quartic-order terms in V_{anharm}. Here, the infrared-active B_{1u} modes fulfill the symmetry requirements for bi-quadratic coupling $Q_{\mathrm{IR,i}}^2 Q_{\mathrm{IR,j}}^2$ and linear-cubic coupling $Q_{\mathrm{IR,i}}^3 Q_{\mathrm{IR,j}}$. Due to the selective resonant excitation of only one polar phonon mode, coupling between three or more different modes is neglected. The corresponding anharmonic term then becomes $V_{anharm} = f_1 Q_{\mathrm{drive}}^2 Q_{\mathrm{IR,2}}^2 + f_2 Q_{\mathrm{drive}}^3 Q_{\mathrm{IR,2}} +$

$f_3 Q_{\mathrm{drive}} Q_{\mathrm{IR},2}^3$. The bi-quadratic term leads to a parametric amplification of the coupled phonons, as becomes apparent from the equations of motion

$$\ddot{Q}_{\mathrm{drive}} + \gamma \dot{Q}_{\mathrm{drive}} + (\omega_{\mathrm{drive}}^2 + 2f_1 Q_{\mathrm{IR},2}^2) Q_{\mathrm{drive}} + 3f_2 Q_{\mathrm{drive}}^2 Q_{\mathrm{IR},2} + f_3 Q_{\mathrm{IR},2}^3 = Z_{\mathrm{drive}}^* Q_{\mathrm{drive}} E_{\mathrm{field}} \quad (1.7)$$

$$\ddot{Q}_{\mathrm{IR},2} + \gamma \dot{Q}_{\mathrm{IR},2} + (\omega_{\mathrm{IR},2}^2 + 2f_1 Q_{\mathrm{drive}}^2) Q_{\mathrm{IR},2} + f_2 Q_{\mathrm{drive}}^3 + 3f_3 Q_{\mathrm{drive}} Q_{\mathrm{IR},2}^2 = 0. \quad (1.8)$$

This parametric amplification is characterized by an exponential scaling of the coupled mode $Q_{\mathrm{IR},2}$ as a function of the driven mode Q_{drive} and a parametric resonance at $\omega_{\mathrm{drive}} = 2 \cdot \omega_{\mathrm{IR},2}$. Figures S4a-d report comprehensive calculations involving coupling between all B_{1u} modes. We scaled the obtained amplitudes by $Z_{B1u,i}^*$ to calculate the polarization induced by each individual mode and convolved the results with the 30-fs time resolution of the experiment. We find agreement with the experimental observations shown in Fig. S5a-d.

S2. Nonlinear phonon-phonon coupling in the symmetry broken state

In a medium with broken inversion symmetry, the strict distinction between zone-center Raman-active and infrared-active phonon modes breaks down. Whilst the YBCO crystal structure is centrosymmetric, recent experimental (Zhao et al. [5]) and theoretical work (Fechner et al. [6]) suggest that a magnetic order develops in the pseudogap phase, which simultaneously breaks time and space inversion symmetry to result in a magnetic point group of *2/m* (Ref. 5) or *mmm'* (Ref. 6). Hence, all phonon modes can be expected to become Raman-active and infrared-active at the same time. Specifically, the A_g modes of the inversion symmetric phase then develop infrared activity, with the symmetry of the B_{1u} modes.

To rule out the appearance of any such Raman-active phonon mode in the second harmonic measurements, sensitive only to polar excitations, we theoretically analyzed the nonlinear phonon-phonon coupling in the magnetic point group of the pseudogap phase.

We utilized the first-principles approach of Ref. 6, where a static spin pattern generates the magnetic point group. In detail, we impose two opposing AFM checkerboard patterns of spins on the Cu atoms within the CuO_2 planes, which lower the *mmm1'* symmetry to *mmm'* for the $YBCO_{6.5}$ unit cell. In addition, we constrained the size of the local spin moment per Cu site to 0.2 μ_B, a value that would be compatible with magnetic probe data [7]. We then calculated the phonon and mode effective charges for $YBCO_{6.5}$ utilizing the procedure described in Section S1.

We find that the mode-effective charges of the former A_g modes are typically three orders of magnitude smaller compared to those of the real infrared-active modes. In detail, the two A_g modes at 3.1 and 3.4 THz develop values of $0.003q_e$ and $0.001q_e$, whilst the effective charge of the B_{1u} polar modes are close to $1q_e$.

We calculated the polarization induced in the $YBCO_{6.5}$ crystal by the (now) infrared active A_g modes in the lattice dynamics simulations, to this end including their mode effective charges. The nonlinear phonon-phonon coupling terms were not changed compared to the centrosymmetric state, since the symmetry breaking to the *mmm'* point group does not produce new phonon-phonon coupling terms.

Figures S4e,f show the time-dependent polarization and the corresponding Fourier transforms that result from the resonantly driven IR modes, the amplified 'real' IR modes (B_{1u}) and the nonlinearly coupled 'new' IR modes (former A_g), the latter magnified by a factor of 2500. Clearly, the polarization induced by the A_g modes is negligible compared to that of the B_{1u} modes, not allowing them to appear in the time-resolved SH intensity measurements.

S3. Theoretical analysis of the Josephson Plasma Polariton

Analysis of the collective modes

Plasmon dispersion in a layered superconductor can be obtained by combining linearized dynamical equations for superflow currents and charges with Maxwell equations for electromagnetic fields [8,9,10,11]. The fundamental degrees of freedom are density fluctuations of the condensate $\delta\rho_{\lambda,\mathrm{i}}(\vec{x})$, the phase of the superconducting order parameter $\phi_{\lambda,\mathrm{i}}(\vec{x})$, and the 4-component vector potential ($V_{\lambda,\mathrm{i}}(\vec{x})$, $A_{\lambda,\mathrm{i},\mathrm{z}}(\vec{x})$ $\vec{A}_{\lambda,\mathrm{i},\vec{x}}(\vec{x})$). Here i corresponds to the index of the unit cell along the c-axis, $\lambda = 1,2$ labels the number of the layer inside the unit cell, and $\vec{x}$ is the in-plane coordinate, which we will omit in the equations below for brevity. While the in-plane components of the vector potential $\vec{A}_{\lambda,\mathrm{i},\vec{x}}(\vec{x})$ are defined within the corresponding layers, $A_{\lambda,\mathrm{i},\mathrm{z}}(\vec{x})$ is defined to be on the links between layers starting on layer $\{\lambda,\mathrm{i}\}$ as shown in Fig. S6.

In linearized hydrodynamics, superflow currents are given by

$$j_{\lambda,\mathrm{i},\vec{x}} = \Lambda_{\mathrm{s}}\left(\partial_{\vec{x}}\phi_{\lambda,\mathrm{i}} - e^{*}A_{\lambda,\mathrm{i},\vec{x}}\right), \tag{3.1}$$

$$j_{\lambda,\mathrm{i},\mathrm{z}} = j_{\mathrm{c}\lambda}\left(\Delta_{\mathrm{z}}\phi_{\lambda,\mathrm{i}} - e^{*}A_{\lambda,\mathrm{i},\mathrm{z}}\right). \tag{3.2}$$

Here $\vec{x}$ denotes the in-plane x, y components and z denotes the c-axis coordinate of the crystal. Coupling to the vector potential is given by the Cooper pair charge, $e^{*} = 2e$, and we work in units where $\hbar = 1$ for the rest of this section. The in-plane components of the superfluid current are defined within individual layers and have continuous gradients. The z component of the current is defined as the Josephson current between adjacent layers and has a lattice gradient which corresponds to the phase difference between adjacent layers,

$$\Delta_z \phi_{\lambda,i} = \begin{cases} (\phi_{2,i} - \phi_{1,i})/d_1, \text{for } \lambda = 1, \\ (\phi_{1,i+1} - \phi_{2,i})/d_2, \text{for } \lambda = 2 \end{cases} \quad (3.3)$$

The coefficient Λ_s is related to the in-plane London penetration length as $\Lambda_s = \frac{\epsilon c^2}{\lambda_L^2 (e^*)^2}$, where $\epsilon = \epsilon_r \epsilon_0$. Physically, it corresponds to the intra-layer superfluid stiffness and is proportional to the condensate density, $\Lambda_{s\lambda} \propto \rho_\lambda$. In linear analysis of the collective modes we can set $\Lambda_{s\lambda}$ to be equal to their equilibrium values since they multiply superfluid velocities, $\vec{v}_{\lambda,i} = \partial_{\vec{x}} \phi_{\lambda,i} - e^* A_{\lambda,i,\vec{x}}$, which are already first order in fluctuations. This is why we omitted the layer index for Λ_s in equation (1). Coefficients $\{j_{c,\lambda}\}$ correspond to interlayer Josephson tunneling couplings and obey $j_{c,\lambda} \propto \sqrt{\rho_1 \rho_2}$. In linearized hydrodynamics we take $j_{c,\lambda}$ to be equal to their equilibrium value and neglect corrections due to $\delta\rho_\lambda$. Both ρ_λ and $j_{c,\lambda}$ can be modified by exciting apical oxygen phonons, which results in phonon-plasmon coupling that will be discussed below. We introduce an effective Hamiltonian that describes plasmon degrees of freedom and show that its equations of motion give the correct equations for light and matter fields.

$$H = H_{pot.} + H_{kin.} + H_{EM.} \quad (3.4)$$

The first term in eqn. (4) describes finite compressibility of Cooper pairs and their coupling to electrostatic potential

$$H_{pot.} = \int d^2x \sum_{i,\lambda} \left\{ \frac{\gamma}{2} \delta\rho_{\lambda,i}^2 + e^* \delta\rho_{\lambda,i} V_{\lambda,i} \right\}. \quad (3.5)$$

Compressibility γ can be related to the Thomas-Fermi length, λ_{TF}, as $\gamma = \frac{\lambda_{TF}^2 (e^*)^2}{\epsilon}$.

The superflow kinetic energy is given by

$$H_{\text{kin.}} = \int d^2x \sum_{i,\lambda} \left\{ \frac{1}{2\Lambda_s} j^2_{\lambda,\text{i},\vec{x}} + \frac{1}{2j_{\text{c},\lambda}} j^2_{\lambda,\text{i},z} \right\}. \tag{3.6}$$

For electromagnetic fields we adopt the Lorenz gauge condition

$$\frac{1}{c^2} \partial_t V_{\lambda,\text{i}} + \partial_{\vec{x}} A_{\lambda,\text{i},\vec{x}} + \Delta_{\text{z}} A_{\lambda,\text{i},\text{z}} = 0 \tag{3.7}$$

then the Hamiltonian for electromagnetic fields is given by

$$\begin{aligned} H_{\text{EM}} = \quad & \int d^2x \left\{ \sum_{i,\lambda} \frac{c^2}{2\epsilon} P^2_{V,\lambda,\text{i}} + \frac{\epsilon}{2} \left(\left(\partial_{\vec{x}} V_{\lambda,\text{i}} \right)^2 + \left(\Delta_{\text{z}} V_{\lambda,\text{i}} \right)^2 \right) \right. \\ & + \frac{1}{2\epsilon} P^2_{A_{\vec{x},\lambda,\text{i}}} + \frac{\epsilon c^2}{2} \left(\left(\partial_{\vec{x}} A_{\lambda,\text{i},\vec{x}} \right)^2 + \left(\Delta_{\text{z}} A_{\lambda,\text{i},\vec{x}} \right)^2 \right) \\ & \left. + \frac{1}{2\epsilon} P^2_{A_{\text{z}},\lambda,\text{i}} + \frac{\epsilon c^2}{2} \left(\left(\partial_{\vec{x}} A_{\lambda,\text{i},\text{z}} \right)^2 + \left(\Delta_{\text{z}} A_{\lambda,\text{i},\text{z}} \right)^2 \right) \right\} \end{aligned} \tag{3.8}$$

Variables $\{P_{\text{V},\lambda,\text{i}}, P_{A_{\vec{x}},\lambda,\text{i}}, P_{\text{A}_{\text{z}},\lambda,\text{i}}\}$ correspond to the conjugate momenta of the scalar and vector potentials, and magnetic permeability $\mu = \mu_{\text{r}}\mu_0$ is included in the speed of light $c^2 = 1/\mu\epsilon$. In Eqn. (8) gradients in the z direction are taken in the lattice form so, for example,

$$\Delta_{\text{z}} A_{\lambda,\text{i},\text{z}} = \begin{cases} \dfrac{A_{1,\text{i},\text{z}}}{d_1} - \dfrac{A_{2,\text{i}-1,\text{z}}}{d_2}, \text{for } \lambda = 1, \\ \dfrac{A_{2,\text{i},\text{z}}}{d_2} - \dfrac{A_{1,\text{i},\text{z}}}{d_1}, \text{for } \lambda = 2 \end{cases} \tag{3.9}$$

We use Heisenberg equations of motion (EOM) for the operators, $\partial_t \hat{O} = i[H, \hat{O}]$, to study dynamics of the fields. In deriving equations of motion we use canonical commutation relations between ρ and ϕ, V and P_{V}, $\vec{A}$ and $P_{\vec{A}}$, i.e. $\left[\rho_{\text{i}}(\vec{x}), \phi_{\text{j}}(\vec{x}\,')\right] = i\delta^2(\vec{x} - \vec{x}\,')\delta_{\text{i,j}}$, etc. EOM for the density and phase operators give the continuity equation and Josephson relation

$$\partial_{\text{t}} \delta\rho_{\lambda,\text{i}} + \partial_{\vec{x}} j_{\lambda,\text{i},\vec{x}} + \Delta_{\text{z}} j_{\lambda,\text{i},\text{z}} = 0. \tag{3.10}$$

$$\partial_{\mathrm{t}}\phi_{\lambda,\mathrm{i}} = -\gamma\delta\rho_{\lambda,\mathrm{i}} - e^{*}V_{\lambda,\mathrm{i}}, \tag{3.11}$$

By combining EOM for the electromagnetic fields ϕ, $\vec{A}$ and their conjugate momenta we obtain Maxwell's equations:

$$\left(\frac{1}{c^2}\partial_{\mathrm{t}}^2 - \partial_{\vec{x}}^2 - \Delta_{\mathrm{z}}^2\right)V_{\lambda,\mathrm{i}} = \frac{e^*}{\epsilon}\delta\rho_{\lambda,\mathrm{i}}, \tag{3.12a}$$

$$\left(\frac{1}{c^2}\partial_{\mathrm{t}}^2 - \partial_{\vec{x}}^2 - \Delta_{\mathrm{z}}^2\right)A_{\lambda,\mathrm{i},\vec{x}} = \frac{1}{c^2}\frac{e^*}{\epsilon}j_{\lambda,\mathrm{i},\vec{x}}, \tag{3.12b}$$

$$\left(\frac{1}{c^2}\partial_{\mathrm{t}}^2 - \partial_{\vec{x}}^2 - \Delta_{\mathrm{z}}^2\right)A_{\lambda,i,\mathrm{z}} = \frac{1}{c^2}\frac{e^*}{\epsilon}j_{\lambda,\mathrm{i},\mathrm{z}} \tag{3.12c}$$

To find collective modes we look for the solutions of equations (10), (11), (12) in the form of plane waves, $\delta\rho_{\lambda,\mathrm{l}}(x,t) = \delta\rho_{\lambda}(q_{\vec{x}}, q_{\mathrm{z}}, \omega)e^{i(q_x x + q_y y + q_z Dl - \omega t)}$, with similar expressions for other variables. It is convenient not to combine EOM for electromagnetic fields and their conjugate variables, so that we have first order linear differential equations of the form $\partial_{\mathrm{t}}\vec{v} = \underline{\boldsymbol{M}}\,\vec{v}$. Matrix $\underline{\boldsymbol{M}}$ contains gradient operators which leads to implicit dependence on momentum $\vec{q}$. We define the characteristic polynomial for $\underline{\boldsymbol{M}}$ as $\chi(\omega) = \det\left|i\omega + \underline{\boldsymbol{M}}\right|$. Due to the Lorenz gauge used in our analysis the characteristic polynomial contains unphysical degrees of freedom. However, gauge constraint (7) guarantees that they do not couple to matter fields and the characteristic polynomial factorizes into physical and unphysical contributions, $\chi(\omega) = \chi_{\mathrm{phys}}(\omega)\chi_{\mathrm{unphys}}(\omega)$. Collective modes of the system can be found by solving the secular equation $\chi_{\mathrm{phys}}(\omega) = 0$. The two lowest energy modes correspond to the Josephson plasmons and their dispersion is shown in Fig. S7.

To express physical quantities in terms of the amplitudes of the plasmon modes we can use eigenvectors $v^{l}_{\{1,2\},q}$ of the secular equation, where components l correspond to $\delta\rho_\lambda$, ϕ_λ, V, $\vec{A}$, etc. Shown in a matrix form:

$$\begin{pmatrix} \rho_\lambda(q) \\ \vdots \\ \phi_\lambda(q) \\ \vdots \end{pmatrix} = \begin{pmatrix} v^{\delta\rho_\lambda}_{1,\mathrm{q}} & \cdots & (v^{\delta\rho_\lambda}_{1,\mathrm{q}})^* & \cdots \\ \vdots & & \vdots & \\ v^{\phi_\lambda}_{1,\mathrm{q}} & & (v^{\phi_\lambda}_{1,\mathrm{q}})^* & \\ \vdots & & \vdots & \end{pmatrix} \cdot \begin{pmatrix} b_1 \\ \vdots \\ b_1^* \\ \vdots \end{pmatrix} \tag{3.13}$$

where b_1 and b_2 are amplitudes of the two plasmon modes oscillating at frequencies corresponding to their dispersion relations. The eigenvectors, $v^{l}_{\{1,2\},\mathrm{q}}$, are defined through the EOM up to a normalization constant. Normalization is fixed through the commutation relations of canonically conjugate pairs, such as $[\rho_\lambda(q), \phi_{\lambda'}(q')] = i\delta_{\mathrm{q,q'}}\delta_{\lambda,\lambda'}$ and commutation relations of the plasmon fields, which should correspond to bosonic creation/annihilation operators $[b_i, b^\dagger] = \delta_{\mathrm{i,j}}$.

To compute the plasmon dispersion curves shown in Fig. S7 and in Fig. 5b of the main text, the following sets of parameters were used for the long and short Josephson junctions.

j_c/(e*) (THz)	ϵ_r	d (Å)
0.75	6.48	9
10.75	2.64	3.5

In addition, we used $s = 2$ Å for the thickness of the superconducting layer, $\lambda_L = 2000$ Å for the London penetration depth and $\mu_{Fermi} = 1$ Å for the Fermi-screening length.

Phonon-plasmon interaction

The apical oxygen phonon is expected to modify the in-plane superfluid stiffness either by changing the in-plane density of carriers or by modifying their hopping. Symmetry of this mode requires that these changes are antisymmetric with respect to the two layers inside one unit cell, so that $\delta\Lambda^{\mathrm{phon}}_{\mathrm{s},\{1,2\}}(t) = \pm\xi Q_{\mathrm{drive}}(t)\Lambda_{\mathrm{s}}$, where coefficient ξ characterizes the coupling strength. Changes of the interlayer Josephson currents arise from changes in the superfluid density $\delta\rho^{\mathrm{phon}}_{\{1,2\}} = \pm\tilde{\xi}\, Q_{\mathrm{drive}}(t)\rho$, which results in $\delta j_{\mathrm{c},\lambda}(t) = -\left(\tilde{\xi}\, Q_{\mathrm{IR}}\right)^2 \frac{j_{\mathrm{c},\lambda}}{2\rho}$. The last equation shows that interlayer Josephson currents couple quadratically to the apical oxygen phonon and lead to four-wave phonon/plasmon mixing. Resonant three wave mixing considered in the main text comes from phonons modifying $\Lambda_{\mathrm{s},\{1,2\}}$ and coupling to the in-plane current.

To derive plasmon dynamics in the presence of excited phonon mode we need to modify equation (6) to include $\delta\Lambda^{\mathrm{phon}}_{\mathrm{s}\lambda}$ arising due to phonons. We find

$$\delta H_{\mathrm{kin.}} = -\xi \sum_i \int d^2x \left\{ \frac{Q_{IR}(t)}{2\Lambda_{\mathrm{s}}} \left(j^2_{1,\mathrm{i},\vec{x}} - j^2_{2,\mathrm{i},\vec{x}}\right)\right\} \tag{3.14}$$

The phonon mode causes a zero momentum three wave parametric process that excites pairs of plasmons at opposite momenta. Resonant processes that satisfy energy matching condition $\omega_{\mathrm{drive}} = \omega_1(q) + \omega_2(-q)$ lead to exponential instability discussed in the main text. After projecting the modified EOM to the two the lowest eigenmodes we find equations for parametrically coupled oscillators

$$\partial_{\mathrm{t}}^2 J_1(q) + 2\gamma_1 \partial_t J_1(q) + \omega_1^2(\vec{q}) J_1(q) = -q_x^2 f(\vec{q}) Q_{\mathrm{drive}}(t) J_2(q), \tag{3.15a}$$

$$\partial_{\mathrm{t}}^2 J_2(q) + 2\gamma_2 \partial_t J_2(q) + \omega_2^2(\vec{q}) J_2(q) = -q_x^2 f(\vec{q}) Q_{\mathrm{drive}}(t) J_1(q) \tag{3.15b}$$

In writing equations (15) we added phenomenological damping constants γ_{i} to describe dissipation due to quasiparticles. Factors of q_{x}^2 in equations (15) originate from the fact that

phonons couple to plasmons through the in-plane superflow kinetic energy. There is also an implicit weaker q dependence in $f(\vec{q})$ arising from projecting the interaction to the plasmon subspace, which can be derived using the $v^{j_{\lambda,\vec{x}}}_{\{1,2\},\mathrm{q}}$ components of the eigenvectors of the secular equation. We also note that inversion symmetry forbids three-mode coupling between the phonon and Josephson plasmons in the same band.

The equation of motion for the polar phonon Q_{drive} now reads

$$\ddot{Q}_{\mathrm{drive}} + 2\gamma_{\mathrm{drive}}\dot{Q}_{\mathrm{drive}} + \omega^2_{\mathrm{drive}}Q_{\mathrm{drive}} = Z^*_{\mathrm{drive}}E_{\mathrm{drive}}(t) - q^2_{\mathrm{x}}J_1J_2\,, \qquad (3.16)$$

We solved the set of coupled equations for the phonon and plasmon dynamics by utilizing a stochastic approach, where we introduced Langevin noise on both, the Josephson plasma and phonon coordinates, to create an incoherent initial state. The final trajectories were then computed by solving the equations of motion one million times with an algorithm based on the Euler-Maruyama method. In addition to the harmonic terms that describe the resonant driving of the polar phonon mode, we also considered higher-order (quartic) phonon anharmonicities.

S4. Doping dependence of the amplified Josephson Plasmon

The SH measurements on the $YBa_2Cu_3O_{6.48}$ sample were complemented by measurements on two differently doped compounds, namely underdoped $YBa_2Cu_3O_{6.65}$ (T_C = 67 K) and optimally doped $YBa_2Cu_3O_{6.92}$ (T_C = 94 K). Figure S8 shows the coherent signal oscillations extracted from the raw data for all three doping levels, measured at 5 K temperature base temperature and 7 MV/cm peak electric field, together with their corresponding Fourier amplitude spectra. The set of nonlinearly coupled phonons (grey peaks) remains unchanged for all three doping levels, whereas the Josephson Plasma frequencies shift with increasing doping to higher frequencies, tracking the blue shift of the Josephson plasma edges in the equilibrium superconducting states [12]. The corresponding frequencies are 2.5 THz and 2.8 THz in

$YBa_2Cu_3O_{6.48}$ and $YBa_2Cu_3O_{6.65}$, respectively (see red peaks in Fig. S8b,d). The Josephson plasmon amplitude was largest in $YBa_2Cu_3O_{6.48}$, smaller in $YBa_2Cu_3O_{6.65}$ and disappeared in optimally doped $YBa_2Cu_3O_{6.92}$. This can be explained by the resonance condition $\omega_{\mathrm{drive}} = \omega_{\mathrm{J1}}(q_{\mathrm{plas}}) + \omega_{\mathrm{J2}}(-q_{\mathrm{plas}})$ for the nonlinear coupling between the resonantly driven phonon and the Josephson plasmons at finite q, which can still be fulfilled in $YBa_2Cu_3O_{6.65}$ ($\omega_{\mathrm{J1}}(0) = 2$ THz, $\omega_{\mathrm{J2}}(0) = 15$ THz) but not in $YBa_2Cu_3O_{6.92}$ ($\omega_{\mathrm{J1}}(0) = 7.5$ THz, $\omega_{\mathrm{J2}}(0) = 30$ THz).

S5. Temperature dependence of the amplified Josephson Plasmon and the phonons

The time-resolved second harmonic intensity $\Delta I_{\mathrm{SH}}(t)$ was measured in the $YBa_2Cu_3O_{6.48}$ and $YBa_2Cu_3O_{6.65}$ samples over a broad range of base temperatures. Figure S9a shows the oscillatory signal contributions in $YBa_2Cu_3O_{6.48}$ for three representative values of 5 K (red), 300 K (light red) and 440 K (grey), extracted by removing the EFISH contribution as described in Section S8 'Materials and Methods'. The corresponding Fourier spectra are shown in Fig. S9b. The amplitude of the 2.5-THz mode in $YBa_2Cu_3O_{6.48}$ was found to extend far above the equilibrium critical temperature T_c (~ 45 K), and to vanish only above T = 400 K. The same measurements allowed to also quantify the temperature dependent amplitude of the amplified phonons $Q_{\mathrm{amplified}}$, by integrating the area under the Fourier transformations in the spectral range between 7 and 11 THz.

The temperature dependent amplitudes of the amplified Josephson Plasmon Polariton, the amplified and driven IR modes, as well as the Raman phonons, shown in Fig. 2h,i of the manuscript and Fig. S10, were obtained by repeating the temperature dependent SH measurements several times and calculating the mean values of the amplitudes to account for systematic errors due to sample drift. Unlike the amplified Josephson plasmon, both the amplified and the driven phonons extend well above the pseudogap temperature T*.

S6. Excitation frequency dependence of the Josephson Plasmon

Our theory predicts the amplification of the Josephson Plasmon Polariton by three-wave mixing with the *c*-axis apical oxygen phonon mode. Hence, we expect the amplification to be enhanced when the mid-infrared excitation pulses are frequency-tuned into resonance with this phonon, where the latter is driven to largest amplitudes.

We tested this prediction by measuring the amplitude of the 2.5 THz mode in $YBa_2Cu_3O_{6.48}$ for different center frequencies of the mid-infrared pulses, keeping the peak electric field constant at ~5 MV/cm. In Fig. S11a,b we plot the oscillatory parts of the recorded time-resolved second harmonic intensity $\Delta I_{SH}(t)$ and the corresponding FFT amplitude spectra. The amplitude J_1 extracted by a time-domain fit (see dashed lines in Fig. S11a) as a function of the excitation frequency and the real part of the YBCO optical conductivity are shown in Fig. S11d. Clearly, the Josephson Plasmon Polariton amplitude increases when the mid-infrared pulses are tuned into resonance with the phonon, supporting the proposed three-wave phonon-plasmon mixing.

Furthermore, Fig. S11c shows that the frequency of the amplified Josephson Plasmon Polariton does not change as function of the mid-infrared center frequency. Given the JPP dispersion, this implies that in the three-wave mixing process, with resonance condition $\omega_{\mathrm{IR}} = \omega_{\mathrm{J1}}(q_{\mathrm{plas}}) + \omega_{\mathrm{J2}}(-q_{\mathrm{plas}})$, the frequency ω_{IR} always takes the same value. Hence, this has to be the eigenfrequency ω_{drive} of the phonon and not the tuned frequency of the mid-infrared excitation pulses.

Together, these two observations show that the amplified JPP amplitude scales with the resonantly enhanced amplitude Q_{drive} of the driven apical oxygen phonon, hence exclude a scenario where the incident mid-infrared light field couples directly to the Josephson plasmon polariton.

S7. Excitation strength dependence of the Josephson Plasmon

The theoretical model presented in this manuscript and discussed in more detail in Ref. 13 predicts parametric amplification of the finite-momentum Josephson plasmon polariton. One validation of this hypothesis was found by fitting the experimental data in Figure 2g (amplitude of the low-frequency plasmon J_1 vs. driven phonon amplitude Q_{drive}) by an exponential scaling function ($J_1 = a \cdot (e^{\alpha Q_{drive} - \beta} - 1)$). The same exponential scaling is also observed for the high-frequency Josephson plasmon J_2. This is evidenced in Fig. S12, where we plot the normalized amplitude J_2 of this mode as a function of Q_{drive}, together with the best fit of $J_1(Q_{drive})$ (dashed line).

S8. Methods

Sample preparation

The samples are detwinned single crystals of $YBa_2Cu_3O_{6+\delta}$ grown in Y-stabilized zirconium crucibles. The hole doping of the Cu-O planes was adjusted by controlling the oxygen content of the CuO chain layer through annealing in flowing O_2 and subsequent rapid quenching [14]. The critical temperatures of the superconducting transitions were determined by dc magnetization measurements (T_c = 45 K for $YBa_2Cu_3O_{6.48}$, T_c = 67 K for $YBa_2Cu_3O_{6.65}$ and T_c = 94 K for $YBa_2Cu_3O_{6.92}$).

For the optical experiments, *ac*-surfaces of the single crystals were polished to optical grade with a final lapping step at 100 nm grid size. The samples were then mounted into an optical cryostat where their temperature could be controlled between 10 and 450 K.

Optical setup

The carrier envelope phase (CEP) stable mid-infrared pump pulses were obtained by mixing the two signal beams from two optical parametric amplifiers, which were seeded by the same white light and pumped by 30-fs pulses at 800 nm wavelength and 1 kHz repetition rate in a 300 μm thick GaSe crystal. The pulses were 150 fs long and centered at 17.5 THz with a bandwidth of 5 THz. An overview of the setup is sketched in Fig. S13a. We used a mid-infrared telescope built from two 90° off-axis parabolic mirrors to focus the pump beam to a spot size of ~60 μm (see Fig. S13b). The driven dynamics in the $YBa_2Cu_3O_{6+x}$ samples were probed by time-delayed linearly polarized replicas of the 800-nm pulses (70 nJ pulse energy), in non-collinear geometry with an angle of ~17° to the normal-incidence mid-infrared pump. This probe beam was focused down to spot-size of 30 μm by a conventional spherical singlet lens and picked up after reflection from the sample by a D-shaped aluminum mirror. Only for the

measurements of the nonlinear scattering angle in the second harmonic generation, the two beams were aligned collinearly onto the sample.

The pump induced polarization rotation of the 800-nm pulses, reflected from the $YBa_2Cu_3O_{6+x}$ samples, was measured by detecting the time-resolved difference signal of two intensity-balanced photodiodes placed behind a half-wave plate and a Wollaston prism.

The light fields generated at the second harmonic frequency (SH) at 400 nm wavelength were separated from the fundamental beam behind the sample by a dichroic mirror and then redirected by UV-enhanced aluminum mirrors to a photo multiplier tube for detection. A prism polarizer was placed as an analyzer in front of the photomultiplier tube (PMT) to detect the 400-nm SH intensity with polarization either along the c axis or the a axis of the $YBa_2Cu_3O_{6.48}$ single crystal. We used a hard coated bandpass filter (390 ± 20 nm) in front of the PMT to prevent any stray light from reaching the detector. For SH polarimetry measurements, the polarization angle of the incoming 800-nm wavelength pulses was rotated by a half-wave plate. The whole setup was enclosed to minimize stray light contamination.

Both schemes probe the material up to a depth of approximately ~0.1 μm, much smaller than the penetration depth of the mid-infrared excitation of about 1.5 μm.

Analysis of the time-resolved SH signals

The measured time-resolved second harmonic intensity $\Delta I_{\mathrm{SH}}(t)$ (see for example Fig. 1c of the manuscript) was fitted by the product of (i) a Gaussian envelope to map the nonlinear optical mixing of pump and probe electric fields at time delay zero (electric field induced second harmonic generation, EFISH) and (ii) a step function of finite width, multiplied by a decaying exponential, i.e. $A(t) = A \cdot (1 + \mathrm{erf}\,((t - t_0)/\sigma)) \cdot \exp\,(-\gamma(t - t_0))$, to describe the exponentially decaying background signal. Subtraction of this slowly varying background revealed the coherent oscillations shown in Figures 2a, 2c and e of the main text for different excitation strengths. The oscillatory signals can be divided into sets of three exponentially

decaying oscillators: the driven polar phonons Q_{drive}, the amplified phonons $Q_{\text{amplified}}$, and the nonlinearly coupled Josephson Plasmon Polaritons J_1 and J_2 (see Fig. S5). These were fitted as $A(t) = A \cdot (1 + \text{erf}((t - t_0)/\sigma)) \cdot \exp(-\gamma(t - t_0)) \cdot \sin(2\pi\Omega t + \phi_0)$. For the phonons, their frequencies Ω_{phonon} were constrained to values measured by linear infrared spectroscopy [15,16].

Heterodyned and homodyned SH detection

The time-resolved second harmonic (SH) signals result from hyper-Raman scattering, induced by the oscillating Josephson plasmon and the infrared-active lattice vibrations, as well as from the electric field induced second harmonic generation (EFISH) prompted by the mid-infrared excitation pulses. These processes can be considered as a nonlinear mixing of the oscillating fields (at frequencies ω_{THz}) with the near-infrared probe pulses (of frequency ω_{IR}), resulting in the generation of sidebands $E_{\text{Q}}(2\omega_{IR} + \omega_{THz})$ close to the second harmonic frequency $2\omega_{IR}$ [17].

Both phase and amplitude of the coherent oscillations are detected by recording the time-delay dependent interference signal of these sidebands

$$I(t) = \int d\omega \left(\left| E_0(2\omega_{IR}) + E_{\text{Q}}(2\omega_{IR} + \omega_{THz}) \cdot \exp(i\omega_{THz} \cdot t) + c.c. \right|^2 \right)$$

$$= I_0 + A(\omega_{THz})\cos(\omega_{THz} \cdot t) + B(\omega_{THz})\cos^2(\omega_{THz} \cdot t),$$

with $E_0(2\omega_{IR})$ a reference oscillator generated either inside the sample or supplied externally.

The homodyned term $B(\omega_{THz})\cos^2(\omega_{THz} \cdot t)$ comprises a rectified and an oscillatory component at $2\omega_{THz}$. The largest contributions descend from the EFISH signal $I_{\text{EFISH,hom.}}(t) = I_{0,\text{EFISH}} \cdot \exp(-2t^2/\sigma_{\text{MIR}}^2) \cdot \cos^2(\omega_{\text{MIR}} \cdot t)$, the driven phonons $I_{\text{Phonon,hom.}}(t) = I_{0,\text{Phonon,hom.}} \cdot \text{erf}(\sqrt{2}t/\sigma_{\text{Phonon}}) \cdot \cos^2(\omega_{\text{Phonon}} \cdot t)$ and the amplified

Josephson plasmon $I_{\mathrm{JP,hom.}}(t) = I_{0,\mathrm{JP,hom.}} \cdot \mathrm{erf}(\sqrt{2}t/\sigma_{\mathrm{JP}}) \cdot \cos^2(\omega_{\mathrm{JP}} \cdot t)$. Here, σ_{MIR} and ω_{MIR} are the temporal width and frequency of the excitation pulse, while $\sigma_{\mathrm{Phonon,JP}}$ and $\omega_{\mathrm{Phonon,JP}}$ denote the rise times and frequencies of the driven phonons and the Josephson plasmon.

The rectified components of the homodyne response produce a slowly-varying background in the SH intensity, illustrated by the simulations shown in Fig. S14a and observed in the experiments (see Figure 1c of the manuscript). The high-frequency homodyned components of the EFISH and the driven phonons ($2\omega_{THz}$ ~ 30-40 THz) are too fast to be resolved by the 30-fs NIR-probe pulses, hence only the plasmon is visible at twice its eigenfrequency ($2\Omega_{\mathrm{JP}}$ ~ 5 THz).

The heterodyned term $A(\omega_{THz})\cos(\omega_{THz} \cdot t)$, oscillating at ω_{THz}, descends from the interference of the light-induced sidebands $E_{\mathrm{Q}}(2\omega_{IR} + \omega_{THz})$ with the reference oscillator $E_0(2\omega_{IR})$. In this case, the time-delay dependent SH intensity is given by the EFISH contribution $I_{\mathrm{EFISH,het.}}(t) = 2E_0E_{0,\mathrm{EFISH}} \cdot \exp(-t^2/\sigma^2) \cdot \cos(\omega_{\mathrm{MIR}} \cdot t)$, the driven phonons $I_{\mathrm{Phonon,het.}}(t) = 2E_0E_{0,\mathrm{Phonon}} \cdot \mathrm{erf}(t/\sigma_{\mathrm{Phonon}}) \cdot \cos(\omega_{\mathrm{Phonon}} \cdot t)$ and the amplified Josephson plasmon $I_{\mathrm{JP,het.}}(t) = 2E_0E_{0,\mathrm{JP}} \cdot \mathrm{erf}(t/\sigma_{\mathrm{JP}}) \cdot \cos(\omega_{\mathrm{JP}} \cdot t)$. Assuming $E_0 \approx 0.10 \cdot E_{0,\mathrm{EFISH}}$ (see the estimation of this ratio below), this heterodyned signal, convolved with the time-resolution of the experiment and added to the homodyne component of Fig. S14a, results in the response shown in Fig. S14b. It agrees well with the experimental data of Figure 1c, indicating that the oscillatory signal contributions are dominated by this heterodyned component.

The dominance of the heterodyned response, detecting the oscillators at their fundamental frequency ω_{THz}, is confirmed by a deeper analysis of the Josephson plasmon dynamics. In Fig. S15h and i, we display time-resolved plasmon dynamics, isolated from all the phonon

contributions via a SH polarimetry analysis (see section below for details), together with its Fourier transform. The heterodyned component at ω_{JP} is four times larger than the homodyned response at $2\omega_{\mathrm{JP}}$.

The reference oscillator $E_0(2\omega_{IR})$, required for the heterodyne detection, is generated by second harmonic generation in the path of the near-infrared probe pulses from the Ti:sapphire amplifier system to the detector. This is evidenced by chopping the probe beam, in that way detecting the total time-resolved intensity I_{SH} instead of the pump induced changes ΔI_{SH}. Fig. S16a shows the result of these measurements, with the pump beam either exciting the sample (red curve) or being blocked in front of it (blue curve). The time delay independent SH intensity of the reference oscillator accounts for approximately 1.5% of the peak of the pump induced SH intensity, which corresponds to $E_0 \approx 0.12 \cdot E_{0,\mathrm{EFISH}}$, confirming the assumption made for the simulation shown in Figure S14**.**

In addition, we replaced the sample with a metallic mirror (black curve) to rule out that this reference is generated by the sample itself (see discussion in and Ref. 5). We confirmed that the reference oscillator, detected with the sample in the optical cryostat, is temperature independent (see Fig. S16b).

Importantly, the oscillations observed in the time-delay dependent SH intensity cannot be explained by changes in the linear reflectivity of the SH reference oscillator arising from the coherent excitation of Raman-active phonons (see Fig. S2a). Those were to be expected of order 1% $\Delta R/R_0$, which is significantly smaller than size of the coherent oscillations in the SH intensity ($\Delta I_{SH}/I_{0,\mathrm{SH}} \sim 1$).

SH polarimetry

To describe the SH polarimetry signals of the symmetry-odd modes in Figure 3, we consider that the instantaneous second harmonic intensity, which is mediated by a third-order susceptibility $\chi^3(\omega_{IR}, \omega_{IR}, \omega_{THz})$, can be described as an effective second-order optical nonlinearity $\chi^2_{\mathrm{eff,t}}(\omega_{IR}, \omega_{IR})$. Hence, the polarization angle dependence can be calculated by considering the full tensorial form of this effective second harmonic generation process

$$P_{\mathrm{i}}^{2\omega} = \sum_{\mathrm{j,k}} \chi^{(2)}_{\mathrm{ijk}} E_{\mathrm{j}}^{\omega} E_{\mathrm{k}}^{\omega} \,. \tag{8.1}$$

Here, the indices i,j,k represent the polarization directions of the polarization *P* and the electric fields *E*. The directions 1,2,3 correspond to the crystal axes *a*,*b*,*c* of the $YBa_2Cu_3O_{6+x}$ unit cell[18].

The nonlinear coefficient χ^2_{ijk} is a third-rank tensor that connects the three interacting fields. Given the Kleinman symmetry condition, the number of independent elements of this tensor can be reduced to 18 elements d_{il} and the most general equation describing second harmonic generation is

$$\begin{pmatrix} P_1^{2\omega} \\ P_2^{2\omega} \\ P_3^{2\omega} \end{pmatrix} = 2 \begin{pmatrix} d_{11} & d_{12} & d_{13} & d_{14} & d_{15} & d_{16} \\ d_{21} & d_{22} & d_{23} & d_{24} & d_{25} & d_{26} \\ d_{31} & d_{32} & d_{33} & d_{34} & d_{35} & d_{36} \end{pmatrix} \begin{pmatrix} E_1^2 \\ E_2^2 \\ E_3^2 \\ 2E_2E_3 \\ 2E_1E_3 \\ 2E_1E_2 \end{pmatrix}. \tag{8.2}$$

Depending on the point group symmetry, the number of independent tensor elements can be further reduced. Given the symmetries of the amplified optical phonons and the Josephson Plasmon Polaritons (see Fig. 5f,g of the manuscript), the relevant point groups for the discussion in this work are *mm2* and *m'*. Their corresponding d_{il} tensors read

$$d_{\mathrm{il}}(mm2) = \begin{pmatrix} 0 & 0 & 0 & 0 & d_{15} & 0 \\ 0 & 0 & 0 & d_{24} & 0 & 0 \\ d_{31} & d_{32} & d_{33} & 0 & 0 & 0 \end{pmatrix} \tag{8.3}$$

and

$$d_{\mathrm{il}}(m') = \begin{pmatrix} d_{11} & d_{12} & d_{13} & 0 & d_{15} & 0 \\ 0 & 0 & 0 & d_{24} & 0 & d_{26} \\ d_{31} & d_{32} & d_{33} & 0 & d_{35} & 0 \end{pmatrix}. \quad (8.4)$$

By choosing an appropriate orientation of the analyzer in front of the detector, we measured the components $P_3^{2\omega}$ (s-analyzer) and $P_1^{2\omega} + P_2^{2\omega}$ (p-analyzer). Equation 4.2 could then be used to fit the shape of the SH polarimetry signals and determine the individual tensor elements d_{il} at any given time delay.

Figure 3 of the manuscript shows data taken with the analyzer oriented along the $YBa_2Cu_3O_{6.48}$ *c* axis (s-analyzer), whilst Fig. S17a plots the measurements taken with the analyzer oriented along the *a* axis (p-analyzer).

Decomposition of the SH polarimetry by frequency filtering

The time-resolved polarimetry signal shown in Fig. 3b of the manuscript, was dissected into the individual contributions of the amplified Josephson plasmon, the amplified phonon and the driven phonons by frequency filtering. To this end, each time trace $\Delta I_{\mathrm{SH}}(t)$ for a given near-infrared polarization angle φ, was subjected to either a low-pass (amplified plasmon), band-pass (amplified phonons) or high-pass (driven phonon) filter. The result of this procedure is shown in Fig. S18. The polarimetry data, shown in Figure 3c-e of the manuscript, were taken from a cut through these angle-dependent data at a constant time delay of 150 fs.

The same analysis was performed on SH polarimetry data with the analyzer oriented along the *a* axis (see Fig. S17b). For one representative time delay the results are shown in Fig. S17c-e. Again, the directly driven phonons (yellow) and the amplified phonons (grey) can be fitted by the χ^2 tensor of the *mm2* point group (dashed lines) relevant for the B_{1u}-symmetry lattice distortions. The sign of the phonon amplitudes at this delay, and hence their phases, are independent of the polarization angle φ. In contrast, the angular dependence of the 2.5 THz

Josephson Plasmon Polariton requires a fit by the χ^2 tensor of a lower-symmetry point group (*m'* or lower) and the amplitude of this mode changes sign as a function of the polarization angle φ.

This result agrees with the symmetry analysis presented in the manuscript for the s-analyzer configuration.

Decomposition of the SH polarimetry by symmetry analysis

The tensorial form of the second harmonic coefficients $d_{il}(mm2)$ and $d_{il}(m')$ for the amplified phonons and the Josephson plasmon, allowed us to decompose the time and angle dependent SH polarimetry signal into three contributions

$$\Delta I_{SH}(t,\varphi) = [A_1(t)\cos^2\varphi + A_2(t)\sin^2\varphi + 2A_3(t)\cos\varphi\sin\varphi]^2 \qquad (8.5)$$

The amplified phonons reduce the symmetry to the point group *mm2*, allowing for two two-lobe patterns that involve the coefficients $A_1(t)$ and $A_2(t)$, see Fig. S15a,d. The Josephson plasmon reduces the point group further to *m'*, generating a 45°-rotated four-lobe pattern proportional to $A_3(t)$, see Fig. S15g, in addition to the two two-lobe patterns proportional to $A_1(t)$ and $A_2(t)$. Hence, the time evolution of the coefficient $A_3(t)$ can be uniquely identified with the dynamics of the amplified Josephson plasmon.

We periodically extended the SH polarimetry signal along the polarization angle axis φ and Fourier filtered these data into circular (q = 0), two-lobe (q = 2) and four-lobe (q = 4) features:

$q = 0$

$$F[\Delta I_{SH}](0) = \tfrac{3}{4}A_1(t)^2 + \tfrac{1}{2}A_1(t)A_2(t) + \tfrac{3}{4}A_2(t)^2 + A_3(t)^2 \qquad (8.6)$$

$q = 2$

$$Re\{F[\Delta I_{SH}](2)\} = \tfrac{1}{2}A_1(t)^2 - \tfrac{1}{2}A_2(t)^2 \qquad (8.7)$$

$$Im\{F[\Delta I_{SH}](2)\} = A_1(t)A_3(t) + A_2(t)A_3(t) \qquad (8.8)$$

$q = 4$

$$Re\{F[\Delta I_{SH}](4)\} = \frac{1}{8}A_1(t)^2 - \frac{1}{4}A_1(t)A_2(t) + \frac{1}{8}A_2(t)^2 - \frac{1}{2}A_3(t)^2 \quad (8.9)$$

$$Im\{F[\Delta I_{SH}](4)\} = \frac{1}{2}A_1(t)A_3(t) - \frac{1}{2}A_2(t)A_3(t) \quad (8.10)$$

This set of five equations allowed us to uniquely determine the coefficients $A_1(t)$, $A_2(t)$, and $A_3(t)$ from the Fourier amplitudes at their specific periodicity. Repeating this procedure for all time delays resulted in the time evolutions of $A_1(t)$, $A_2(t)$, and $A_3(t)$ plotted in Fig. S15 together with their Fourier transforms.

Momentum-resolved detection of the Josephson Plasmon Polariton

In the SH measurement, the 400-nm wavelength light is generated in a thin layer *l* of about 100 nm below the sample surface. The finite in-plane momentum q_{JP} of the amplified Josephson Plasmon Polariton leads to a deflection of the second harmonic light with respect to the specular reflection. The spatial distribution of the emitted radiation was determined by taking second harmonic intensity measurements $\Delta I_{\mathrm{SH}}(t)$ at different positions of a 200-µm slit, which was scanned across the re-collimated reflected beam 100 mm after the sample. The amplitudes of the frequency-filtered 2.5-THz JPP and the amplified phonon contributions are plotted as a function of the slit position in Fig. S19b,c, together with the EFISH amplitude at time zero shown in Fig. S19a**.** The momentum transfer was calculated from the deflection angle $\Delta\theta$ by

$$q_{\mathrm{x}} = \sqrt{\varepsilon_\infty}\tan(\Delta\theta)k_{400},$$

where k_{400} is the vacuum wavenumber of the 400-nm light. While both the EFISH and amplified phonon contributions are symmetric and peak at zero in-plane momentum transfer q_{x}, the plasmon response is asymmetric and peaks at a finite momentum q_{x} = 190 cm^{-1}.

The momentum distribution of the Josephson Plasmon Polariton, shown in Fig. 4d of the main text, was then obtained by deconvolving the measured JPP profile (Fig. S19c) from the divergence of the probe beam. To this end, consistent with our theoretical model, two constrained Gaussian profiles, with equal but opposite abscissa offsets and same widths, were fitted to the data. The best fit was deconvolved with the Gaussian profile of the undeflected second harmonic beam, which is accessible from the momentum dependent EFISH signal due to the collinearity between the incident mid-IR excitation and 800-nm probe beams in these measurements. Constrained in this way, the deconvolution yielded a unique result which describes the data, shown in Fig. 4d. The error-bars of the deconvoluted data points are determined by the deviation of the least squares fit to the data points. Note that the 190-cm^{-1} momentum shift is already clearly visible in the raw data shown in Fig. S19c.

SUPPLEMENTAL FIGURES

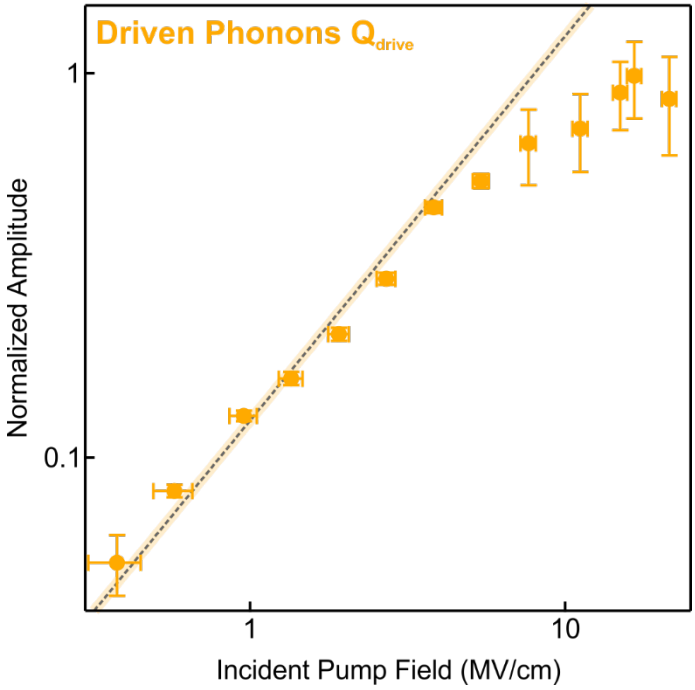

Figure S1: Measured dependence of the driven phonon amplitude Q_{drive} as a function of the incident peak electric field. The dashed black line is a linear fit, $Q_{\mathrm{drive}} = aE_{\mathrm{field}}$. Error bars represent the standard deviation σ of the amplitudes extracted by numerical fits.

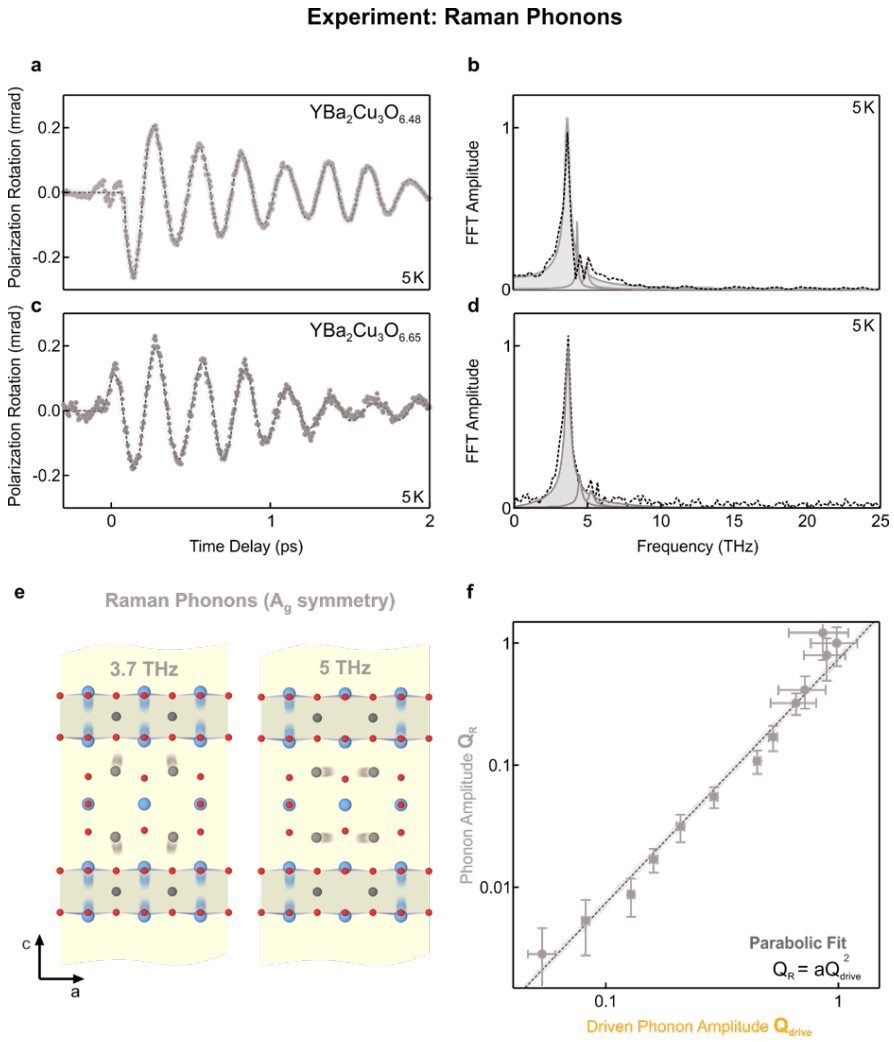

Figure S2: Coherent component of the polarization rotation signal of $YBa_2Cu_3O_{6.48}$ in panel **a** and of $YBa_2Cu_3O_{6.65}$ in panel **c** both recorded at an excitation field of ~ 7MV/cm. The dashed lines are a time domain fit with several exponentially decaying oscillators. The corresponding Fourier amplitude spectra are shown in panel **b** and **d**, respectively. The individual oscillators of the time domain fits are shown as grey peaks. **e** Real space motion of the two dominant Raman modes at 3.7 and 5 THz determined by ab-initio methods. **f**, Measured excitation strength dependence of the amplitude of the 3.7 THz mode as a function of the amplitude of the driven apical oxygen vibration The dashed black line is a parabolic fit, $Q_{\mathrm{R}} = aQ_{\mathrm{drive}}^2$. Error bars represent the standard deviation σ of the amplitudes extracted by numerical fits.

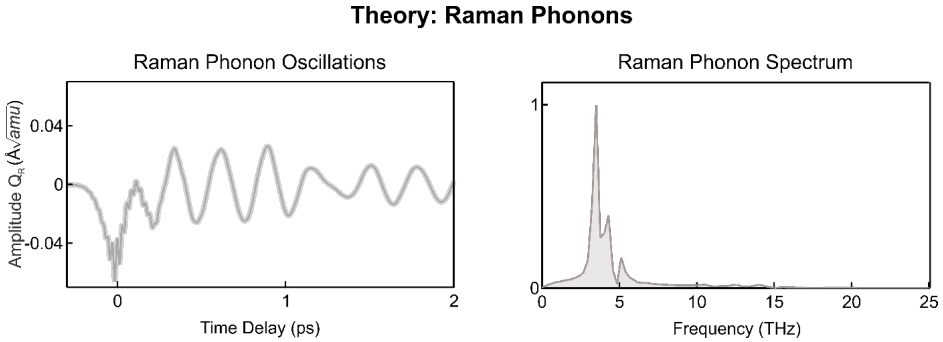

Figure S3: Simulated coherent oscillations of the Raman modes excited by ionic Raman scattering due to their third-order nonlinear coupling to the resonantly driven apical oxygen phonons. The corresponding frequency spectrum is shown in the right panel and displays the same dominant response at 3.7 and 5 THz as observed in the experiment.

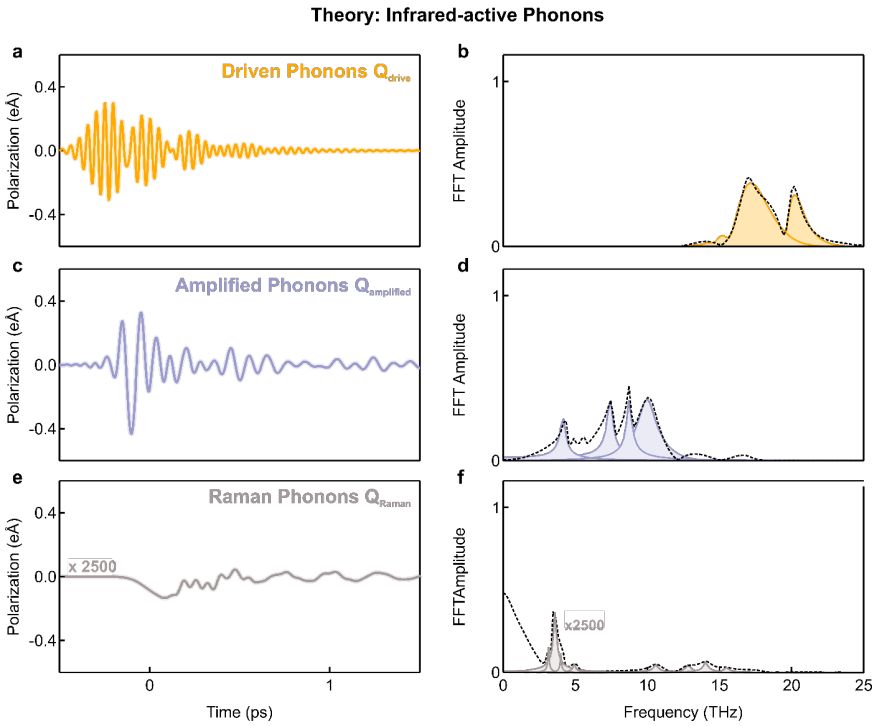

Figure S4: a Simulated polarization induced by the coherent oscillations of the resonantly driven apical oxygen vibrations Q_{drive} (yellow). **b**, The corresponding Fourier amplitude spectrum exhibits two peaks at 17 and 20 THz (dashed line). The individual phonon responses are shown as yellow peaks, whilst the total response is drawn as a dashed black line. **c**, Simulated polarization induced by the coherent oscillations of the nonlinearly coupled (amplified) infrared-active vibrations $Q_{amplified}$ at 4, 6, 8 and 10 THz (grey), which are driven through fourth-order nonlinear coupling to the resonantly driven apical oxygen phonons. **d**, The Fourier amplitude spectrum (dashed black) can be dissected into the response of the individual modes, which are shown as shaded grey peaks. The response agrees well with the experimental data. **e**, Simulated polarization of the nonlinearly coupled A_g Raman phonons when artificially lowering the point group symmetry of $YBCO_{6.5}$ to mmm', magnified by a factor of 2,500 relative to the panels a and c. **f**, The total Fourier amplitude spectrum (dashed line) is plotted together with the individual modes that are shown as shaded peaks (again magnified by 2,500).

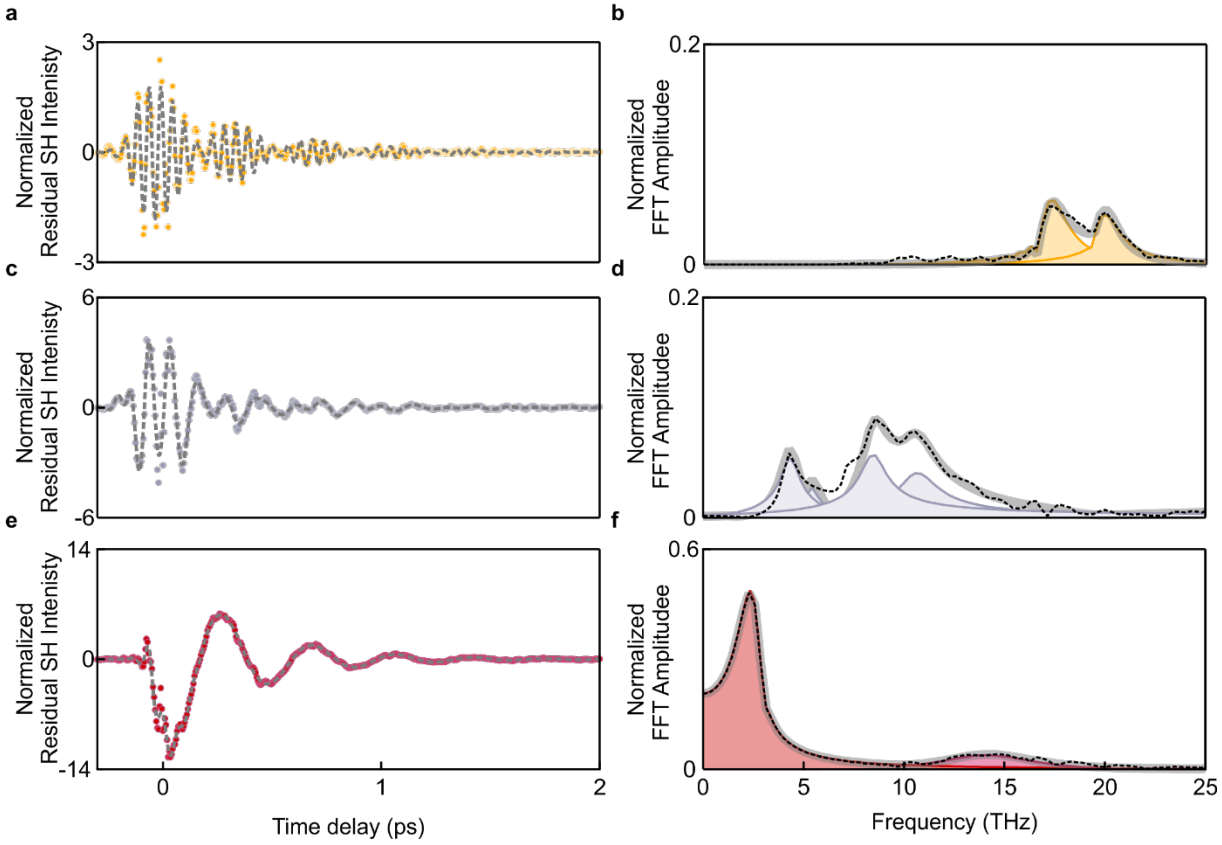

Figure S5: Coherent oscillations in the time-resolved second harmonic intensity $\Delta I_{\mathrm{SH}}(t)$ from $YBa_2Cu_3O_{6.48}$, as shown in Fig. 2e of the main text for 7MV/cm excitation at 5 K, divided into three contributions and shown together with their Fourier amplitude spectra. Panels **a,b** show the driven apical oxygen phonons, panels **c**,**d** show the amplified infrared-active phonons, and panels **e**,**f** show the Josephson Plasma Polariton modes. Experimental phonon oscillations (yellow and grey dots in a and c, respectively) are fitted by oscillators with frequencies constrained by infrared spectroscopy data (dashed lines). Oscillations of the two Josephson plasma modes (experimental data as red dots in e) are best fitted by two oscillators at 2.5 and 14 THz (dashed line). In the Fourier amplitude spectra, the colored peaks highlight the respective contributions.

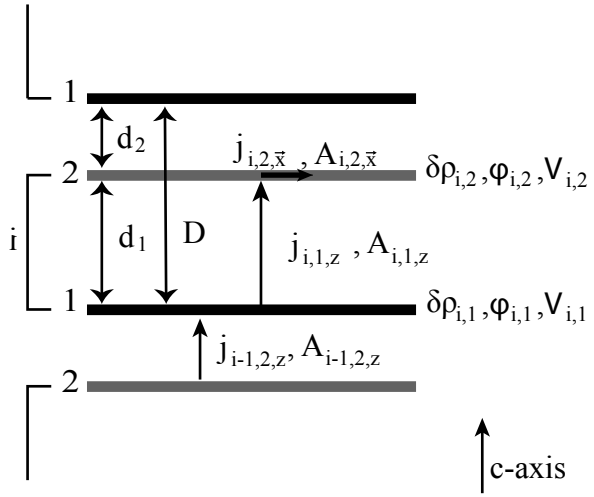

Figure S6: Schematic drawing of a bilayer superconductor. Variables $\delta\rho_{i,\lambda}$, $\phi_{i,\lambda}$, $j_{i,\lambda,\vec{x}}$, and $A_{i,\lambda,\vec{x}}$ are defined within layer λ in unit cell i and describe condensate density fluctuations, phase of the order parameter, parallel component of the superfluid current, electrostatic potential, and in-plane vector potential respectively. Variables $j_{i,\lambda,z}$, and $A_{i,\lambda,z}$ are defined between the layers and correspond to interlayer Josephson current and out of plane component of the vector potential, respectively.

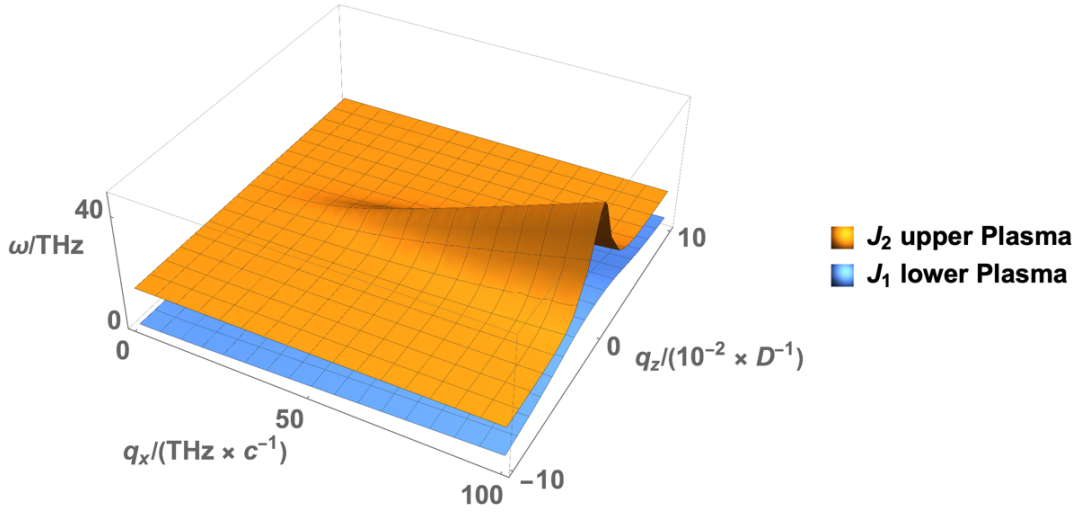

Figure S7: Dispersion relation of the two lowest energy modes of equations (10)-(12) in the $\{q_x, q_z\}$-plane. At $q_z = 0$, the upper plasmon is strongly hybridized with the original photon mode. This results in the energy of the mode increasing rapidly along the q_x axis with the slope approaching the speed of light. Away from $q_z = 0$ strong mixing with the photon is absent and the frequency of the mode decreases with increasing q_x.

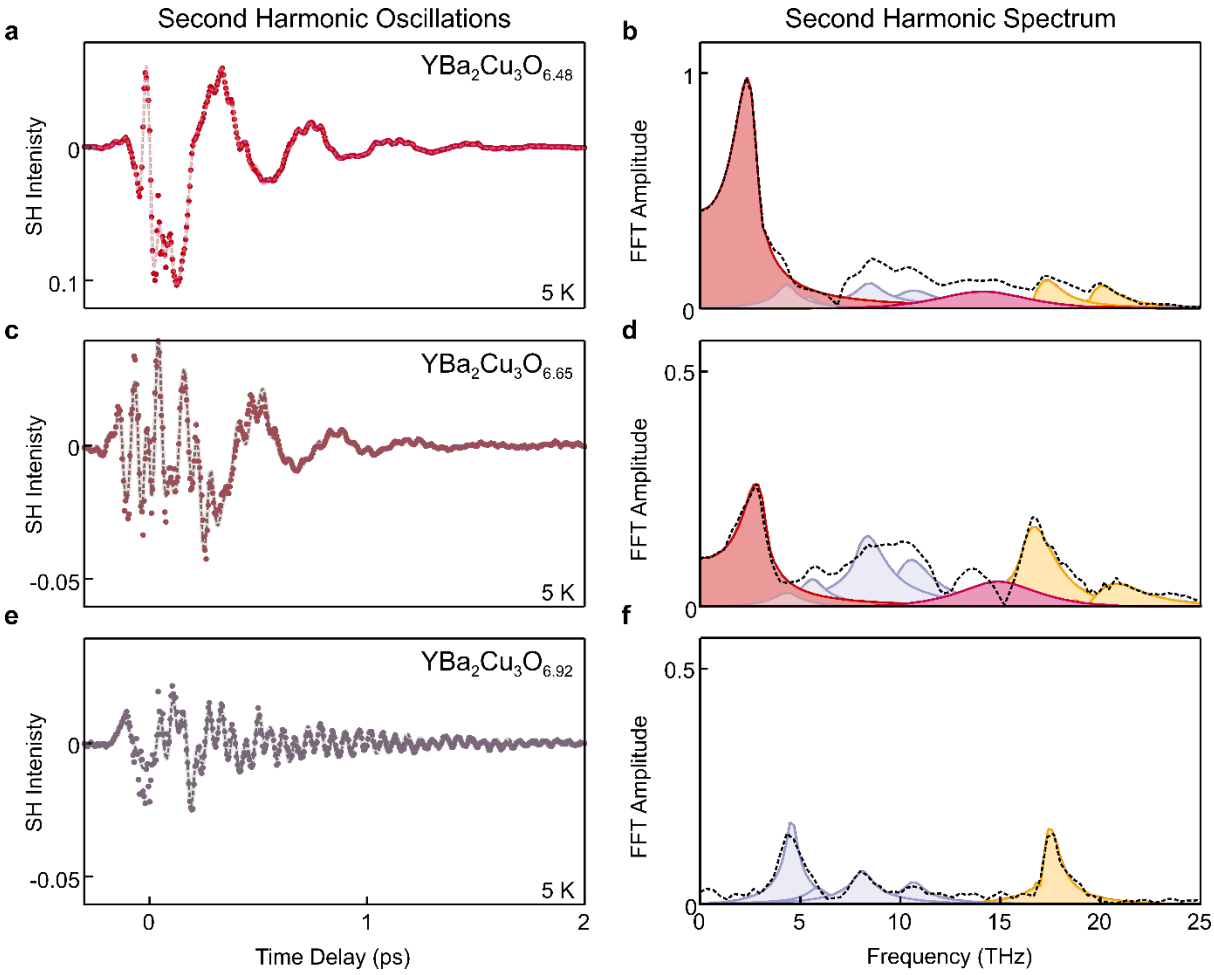

Figure S8: Coherent oscillations in the time delay dependent second harmonic intensity of **a** $YBa_2Cu_3O_{6.48}$, **c** $YBa_2Cu_3O_{6.65}$ and **e** $YBa_2Cu_3O_{6.92}$, measured in the superconducting state at 5 K, together with corresponding Fourier amplitude spectra in **b, d, f**. Experimental data are plotted as red dots in panels a, c, e, together with the best fits to the data (light grey dashed lines) and the dominating low-frequency Josephson plasmon contribution (black solid line). The Fourier amplitude spectra include Josephson plasmons as red and magenta peaks, resonantly driven apical oxygen phonons as yellow peaks, and the nonlinear coupled infrared active phonons as grey peaks. Note the absence of the Josephson plasma oscillations in $YBa_2Cu_3O_{6.92}$. All experiments were performed with a peak electric field strength of 7 MV/cm.

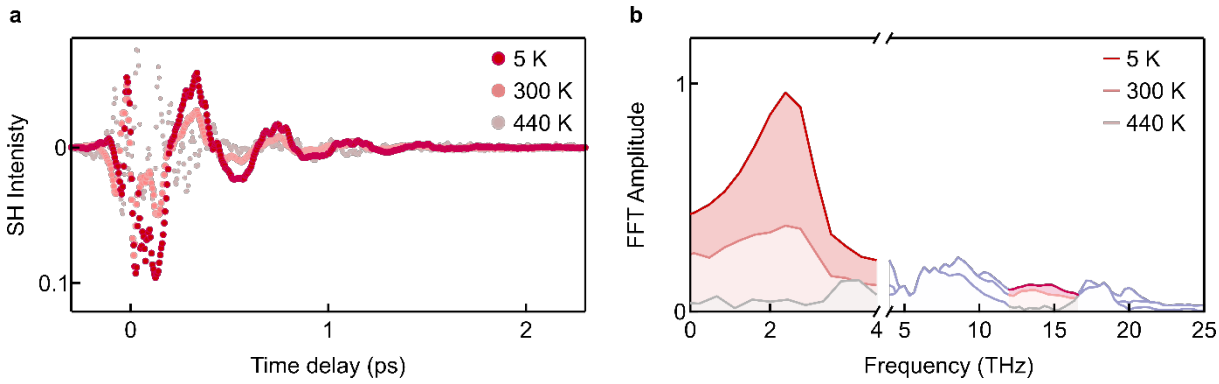

Figure S9: a Temperature dependent coherent oscillation of the SH intensity in $YBa_2Cu_3O_{6.48}$ for three base temperatures of 5 K (red), 300 K (light red) and 440K (grey). Their corresponding FFT amplitude spectra are shown in panel **b**. The shaded areas highlight the spectral regions of the amplified Josephson plasma modes.

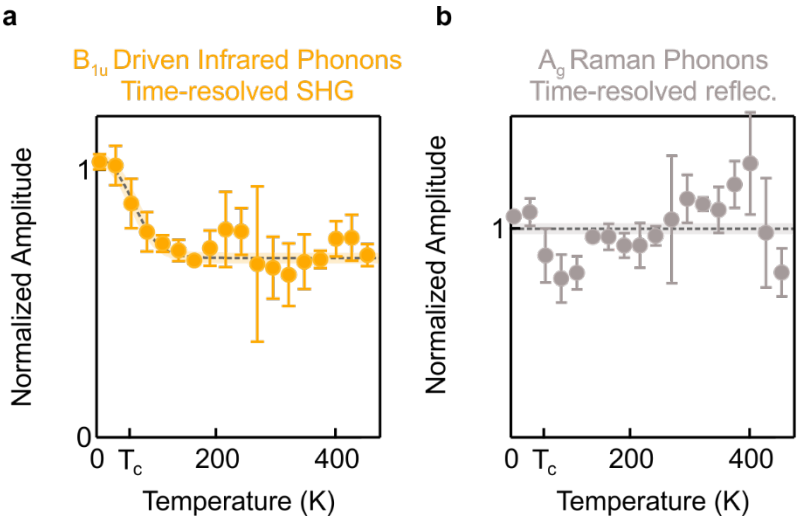

Figure S10: Temperature dependent amplitudes of the driven infrared-active phonon (**a**, taken from time-resolved second harmonic measurements) and of the nonlinearly coupled A_g Raman phonons (**b**, taken from time-resolved reflectivity measurements). The dashed lines are a guide to the eye. Error bars represent the standard deviation σ of the amplitudes obtained by repeating the experiment under equivalent conditions. All experiments were performed with a peak field strength of ~7 MV/cm.

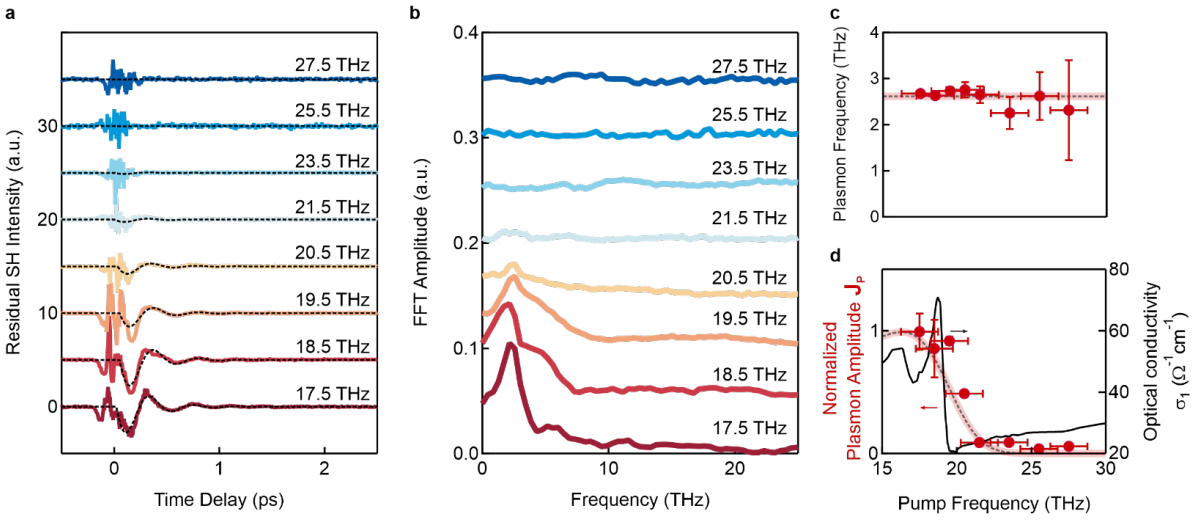

Figure S11: a and **b** show the coherent oscillations of the SH intensity and the corresponding FFT amplitudes measured in $YBa_2Cu_3O_{6.48}$ at different mid-infrared frequencies while peak electric field of ~5 MV/cm. **c** and **d**, Frequency and amplitude of the low-frequency Josephson Plasmon Polariton (red data points) extracted from a time-domain fit to the data shown in panel a (dashed lines). The amplitude increases towards the resonance of the optically excited apical oxygen lattice vibration. The real part of the optical conductivity is drawn as solid black line, and as a dashed line when convolved with the bandwidth of the excitation pulses. Error bars represent the standard deviation σ of the JPP amplitudes extracted by numerical fits. Horizontal error bars represent the standard deviation σ of the center wavelength determined by electro-optic sampling.

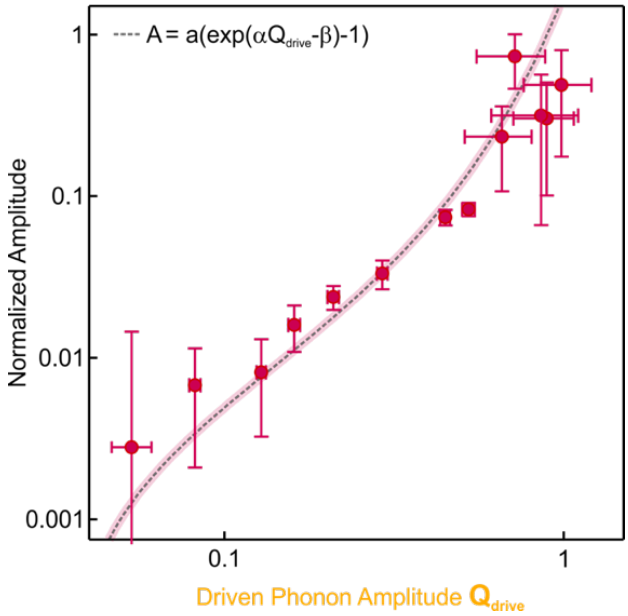

Figure S12: Measured amplitude J_2 of the amplified 14-THz Josephson plasmon polariton in $YBa_2Cu_3O_{6.48}$ as a function of the driven apical oxygen vibration amplitude Q_{drive}. The dashed line is the exponential fit obtained from the dependence of the low-frequency plasmon J_1 as a function of Q_{drive}, highlighting similar scaling of the low- and high-frequency Josephson plasmons.

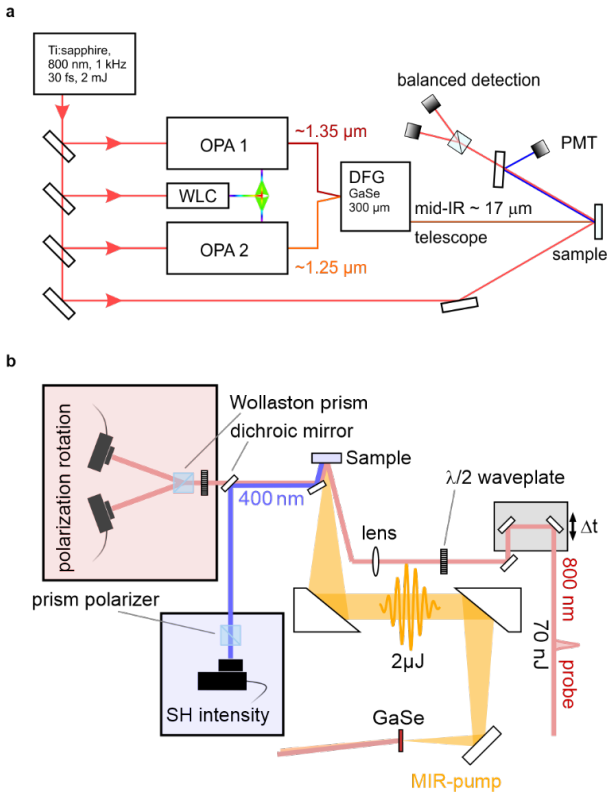

Figure S13: a, Sketch of the experimental setup used for the generation of strong-field mid-infrared pulses and time-resolved optical detection of the linear and nonlinear sample response. The mid-infrared pump pulses were obtained by mixing the two signal beams from two optical parametric amplifiers (OPA), which were seeded by the same white light (WLC) and pumped by 30-fs pulses at 800 nm wavelength from a 1 kHz repetition rate Ti:sapphire amplifier system. The driven dynamics in the $YBa_2Cu_3O_{6+x}$ samples were probed by time-delayed linearly polarized replicas of the 800-nm (70 nJ) pulses, in non-collinear geometry to the normal-incidence mid-infrared pump. The reflected fundamental (800 nm) and second harmonic (400 nm) beams were separated by a dichroic mirror and detected separately. The polarization of the SH beam was analyzed by a prism polarizer. **b**, Detailed Sketch of the experiment detection geometry.

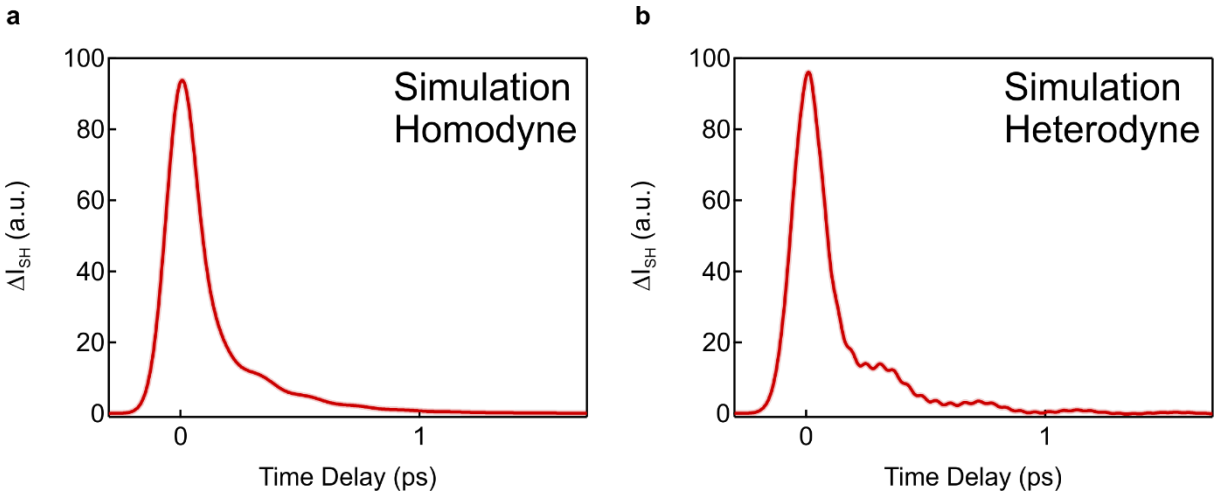

Figure S14: a, Simulated changes ΔI_{SH} of the SH intensity taking into account only the homodyned signal contribution. **b**, Simulated changes ΔI_{SH} of the SH intensity signal including both the heterodyne and the homodyne components, with a static background (reference oscillator) of 1% of the peak SH intensity. Both curves were convolved with the experimental time resolution of 30 fs.

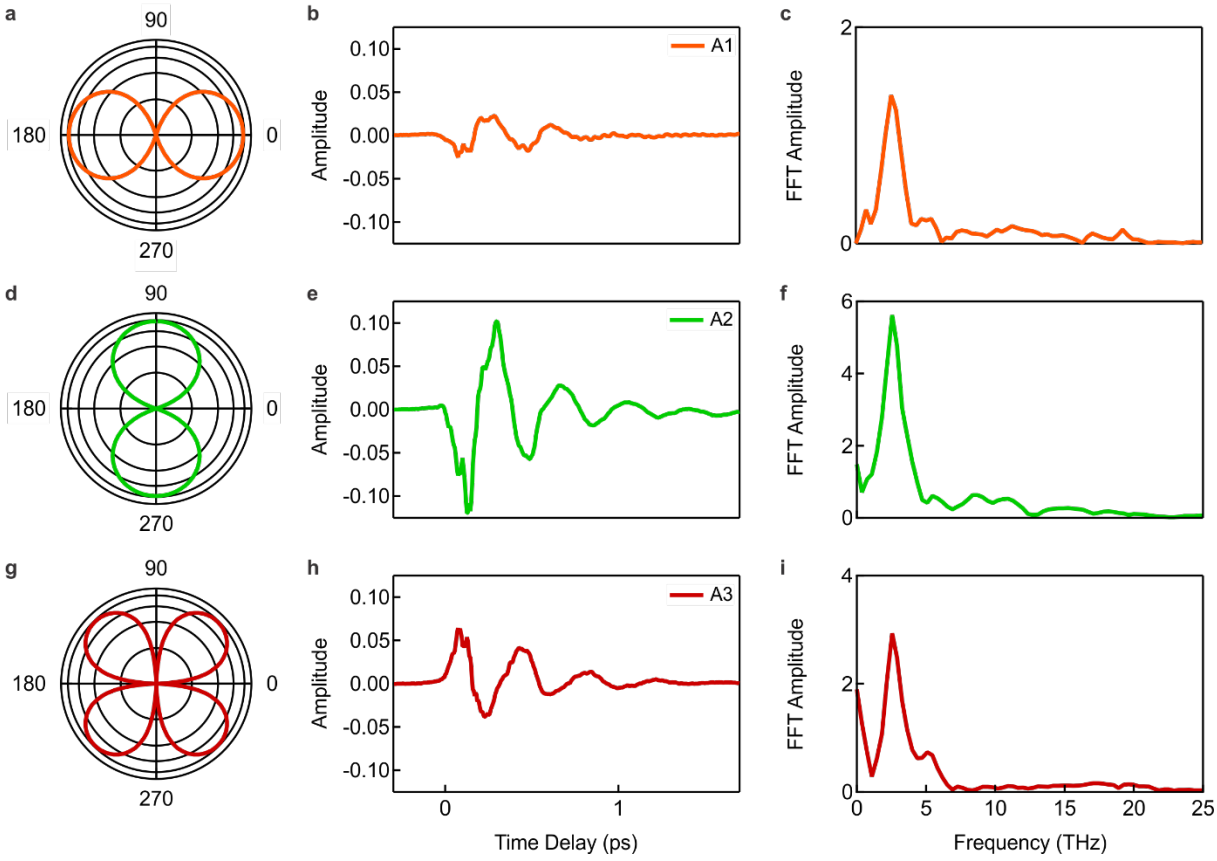

Figure S15: a, **d** and **g,** Angular dependence of the SH polarimetry signal contributions, associated with the three coefficients $A_1(t)$, $A_2(t)$ and $A_3(t)$, that result from the symmetry reduction of $YBCO_{6.5}$ to the $mm2$ (phonons) and m' (Josephson plasmon) point groups. Panels **b**,**e**,**h** and **c**,**f**,**i**, plot the corresponding temporal evolution, extracted from the signal in Figure 3b of the manuscript, as well as their Fourier transforms, respectively. See Methods section 'SH polarimetry' for details of the symmetry analysis used to filter the different contributions.

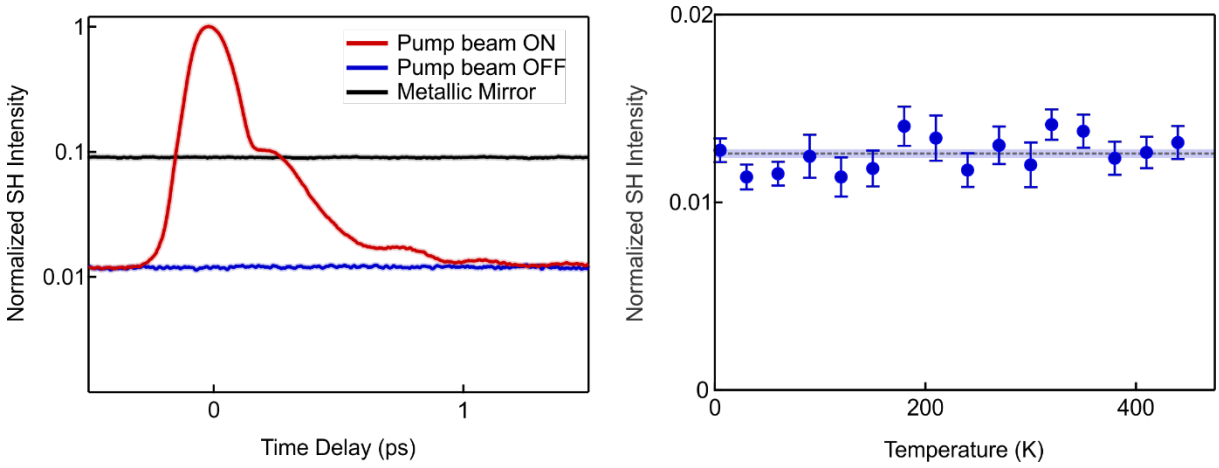

Figure S16: a, Normalized total SH intensity measured with the pump and probe beams incident on the sample (red line), with only the probe beam present (blue line), and with the sample replaced with a metallic mirror (black line). **b**, Temperature dependence of the time delay independent SH background detected with the YBCO sample in place (blue line in **a**). Error bars represent the standard deviation σ of the amplitudes obtained by repeating the experiment under equivalent conditions.

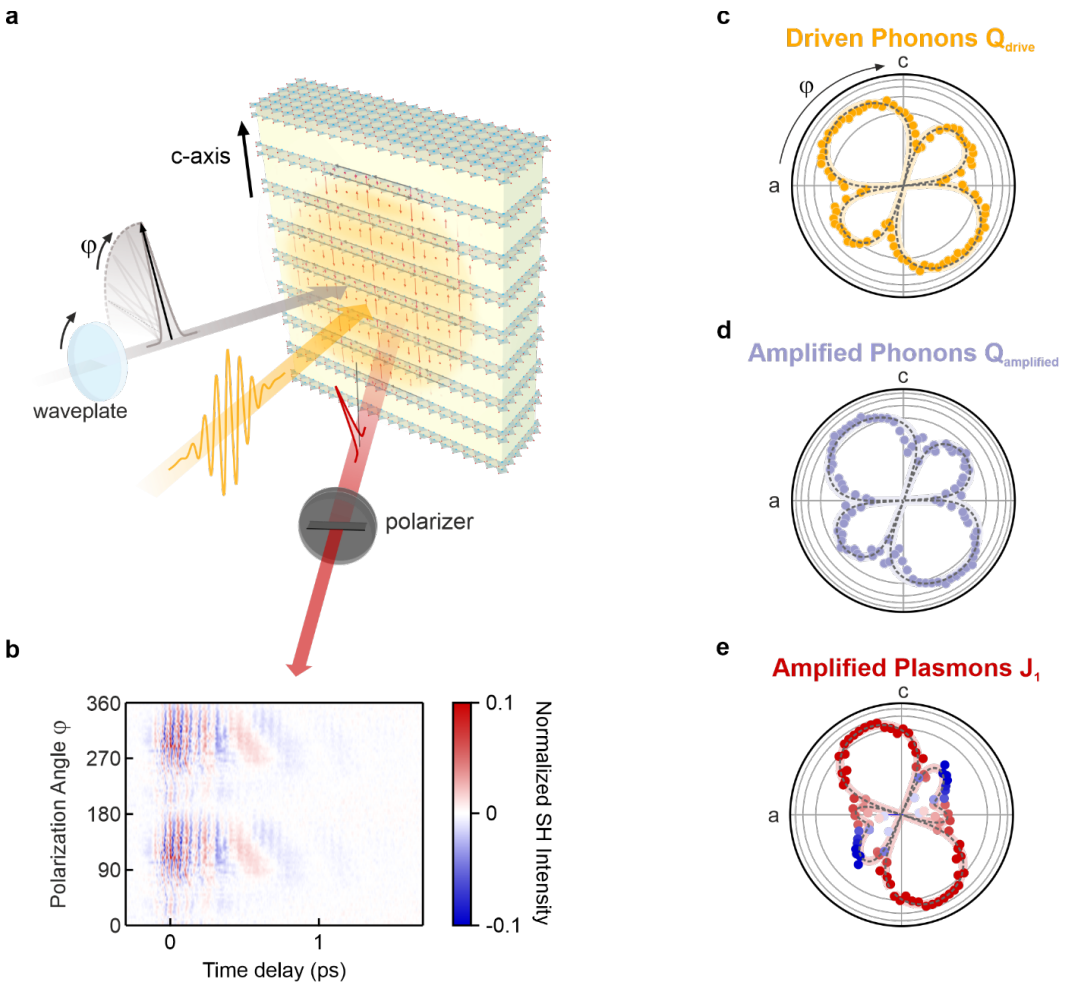

Figure S17: a, Sketch of the SH polarimetry experimental geometry for a horizontal analyzer alignement. **b**, SH signal as a function of polarization angle and pump-probe time delay, measured at room temperature. **c**,**d** and **e**, Normalized SH polarimetry signal of the driven phonons (yellow dots), amplified phonons (grey dots) and amplified Josephson Plasmon Polariton (red and blue dots) for an analyzer oriented along the crystal *a*-axis, around a time-delay t = 500 fs. The signal of the two sets of phonons can be reproduced by a fit to a *mm2* point group symmetry (dashed line) and the phase of the oscillations is polarization angle φ independent. The signal of the amplified Josephson Plasmon Polariton agrees with a fit to point group *m* (dashed line). The phase of the polarimetry signal is indicated by the red and blue color-coding. The SH polarimetry data was recorded at room temperature with at peak electric field of ~5 MV/cm.

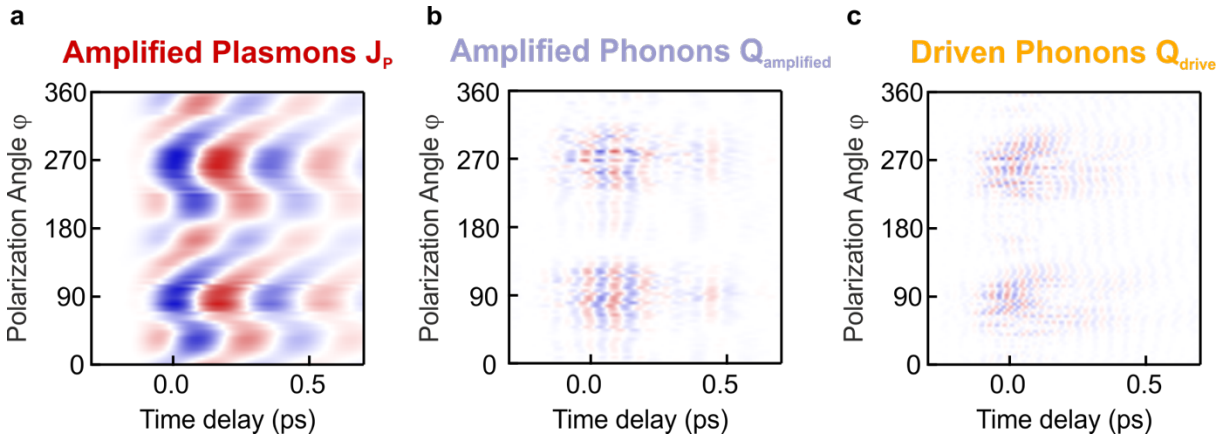

Figure S18: Normalized polarimetry signals of the amplified plasmon, the amplified phonon and the driven phonon, extracted from Figure 3b of the manuscript by applying **a**, a low-pass filter, **b**, a band-pass filter and **c,** a high-pass filter, respectively.

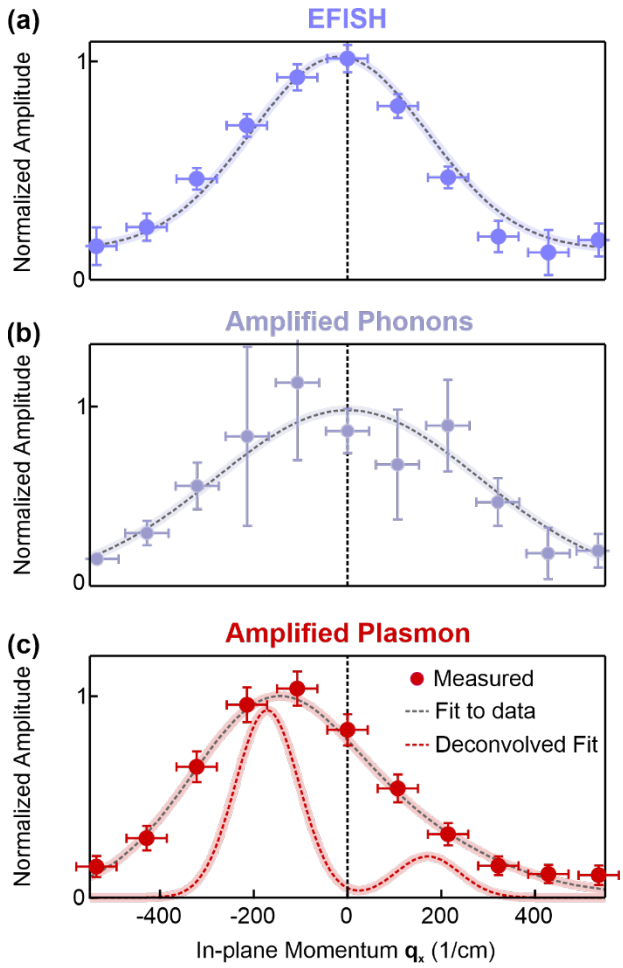

Figure S19: a In-plane momentum distribution of the EFISH-component, **b** amplitude of the amplified phonon oscillations and **c** coherent Josephson Plasmon Polariton oscillations, as measured in the experiment sketched in Figure 4a of the main text. Data points are shown as blue, grey and red symbols. The Gaussian fit to the EFISH data, shown as a dashed grey line in **a**, reveals the divergence of the second harmonic beam. In panel **c**, the fit to the raw data and of the Josephson Plasmon Polariton amplitude and its $\omega_{\mathrm{IR}} = \omega_{\mathrm{J1}}(q_{\mathrm{JP}}) + \omega_{\mathrm{J2}}(-q_{\mathrm{JP}})$ deconvolution are plotted as dashed grey and red lines, respectively. Error bars represent the standard deviation σ of the amplitudes extracted by numerical fits. Horizontal error bars represent the standard deviation σ due to the finite width of the measurement slit. The data was recorded at room temperature with a peak field of ~5 MV/cm.

References

[1] M. Fechner and N. A. Spaldin, Effects of intense optical phonon pumping on the structure and electronic properties of yttrium barium copper oxide. Phys. Rev. B **94**, 134307 (2016).

[2] D. M. Juraschek, M. Fechner, and N. A. Spaldin, Ultrafast Structure Switching through Nonlinear Phononics. Phys. Rev. Lett. **118**, 054101 (2017).

[3] R. Mankowsky, A. Subedi, M. Först, S. Mariager, M. Chollet, H. Lemke, J. S. Robinson, J. M. Glownia, M. P. Minitti, A. Frano, M. Fechner, N. A. Spaldin, T. Loew, B. Keimer, A. Georges and A. Cavalleri, Nonlinear lattice dynamics as a basis for enhanced superconductivity in $YBa_2Cu_3O_{6.5}$. Nature **516**, 71 (2014).

[4] M. Först, C. Manzoni, S. Kaiser, Y. Tomioka, Y. Tokura, R. Merlin and A. Cavalleri, Nonlinear phononics as an ultrafast route to lattice control. Nature Physics **7**, 854 (2011).

[5] L. Zhao, C. A. Belvin, R. Liang, D. A. Bonn, W. N. Hardy, N. P. Armitage, and D. Hsieh, A global inversion-symmetry-broken phase inside the pseudogap region of $YBa_2Cu_3O_y$. Nature Physics **13**, 250 (2016).

[6] M. Fechner, M. J. A. Fierz, F. Thöle, U. Staub, and N. A. Spaldin. Quasistatic magnetoelectric multipoles as order parameter for pseudogap phase in cuprate superconductors. Physical Review B **93**, 174419 (2016).

[7] B. Fauqué, Y. Sidis, V. Hinkov, S. Pailhès, C.T. Lin, X. Chaud, and P. Bourges. Magnetic order in the pseudogap phase of high-TC superconductors. Phys. Rev. Lett. **96**, 197001 (2006).

[8] L. N. Bulaevskii, M. Zamora, D. Baeriswyl, H. Beck, and John R. Clem. Time-dependent equations for phase differences and a collective mode in Josephson-coupled layered superconductors. Phys. Rev. B **50**, 12831(1994).

[9] T. Koyama and M. Tachiki. I-v characteristics of Josephson-coupled layered superconductors with longitudinal plasma excitations. Phys. Rev. B **54**, 16183 (1996).

[10] J. Okamoto, A. Cavalleri, and L. Mathey. Theory of enhanced interlayer tunneling in optically driven high-T_c superconductors. Phys. Rev. Lett. **117**, 227001(2016).

[11] J. Okamoto, W. Hu, A. Cavalleri, and L. Mathey, Transiently enhanced interlayer tunneling in optically driven high-T_c superconductors. Phys. Rev. B **96**, 144505 (2017).

[12] S. Kaiser, C. R. Hunt, D. Nicoletti, W. Hu, I. Gierz, H. Y. Liu, M. Le Tacon, T. Loew, D. Haug, B. Keimer, and A. Cavalleri, Optically induced coherent transport far above T_c in underdoped $YBa_2Cu_3O_{6+\delta}$. Physical Review B **89**, 184516 (2014).

[13] M.H. Michael, A. von Hoegen, M. Fechner, M. Först, A. Cavalleri and E. Demler, Parametric resonance of Josephson plasma waves: A theory for optically amplified interlayer superconductivity in $YBa_2Cu_3O_{6+x}$. Physical Review B **102**, 174505 (2020).

[14] S. I. Schlachter et al., Pressure effect and specific heat of $RBa_2Cu_3O_x$ at distinct charge carrier concentrations: Possible influence of stripes. Int. J. Mod. Phys. B **14**, 3673 (2000).

[15] C.C. Homes, T. Timusk, and D.A. Bonn, R. Liang and W.N. Hardy, Optical phonons polarized along the c axis of YBa2Cu3O6+x, for x = 0.5 → 0.95. Canadian Journal of Physics **73**, 663 (1995).

[16] J. Schützmann, S. Tajima, S. Miyamoto, Y. Sato and R. Hauff, Doping and temperature dependence of c-axis optical phonons in $YBa_2Cu_3O_y$ single crystals. *Physical Review B* 52, 13665 (1995).

[17] A. von Hoegen, R. Mankowsky, M. Fechner, M. Först, A. Cavalleri, Probing the interatomic potential of solids with strong-field nonlinear phononics. *Nature* 555, 79-82 (2018).

[18] S. A. Denev, T. T. A. Lummen, E. Barnes, A. Kumar and V. Gopalan. Probing Ferroelectrics Using Optical Second Harmonic Generation. J. Am. Ceram. Soc., 94 [9] 2699–2727 (2011).